

RESEARCH ARTICLE SUMMARY

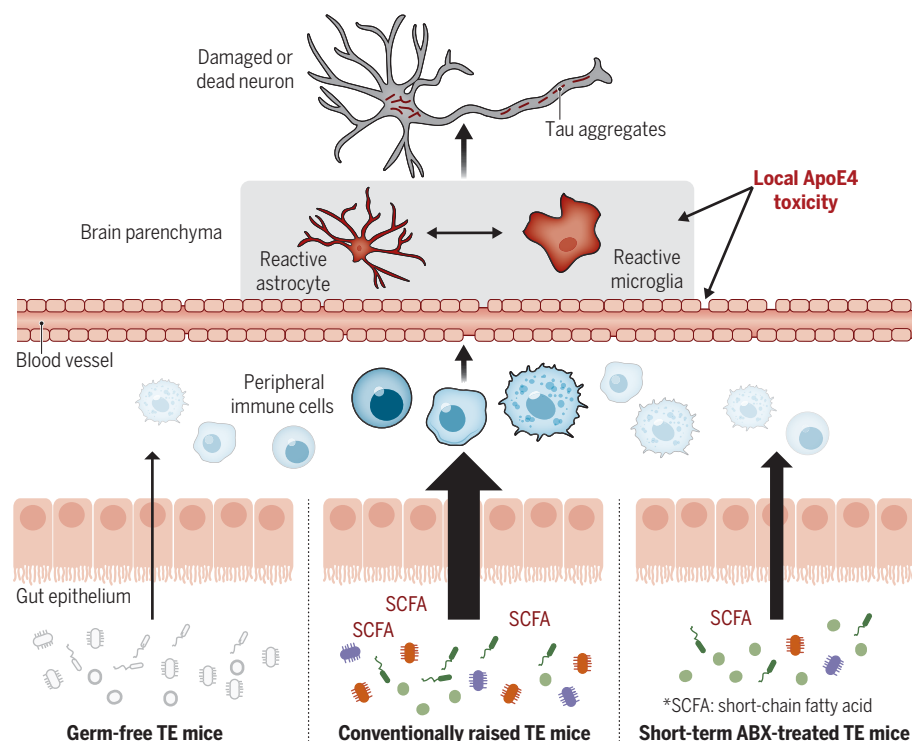
NEURODEGENERATION

ApoE isoform- and microbiota-dependent progression of neurodegeneration in a mouse model of tauopathy

Dong-oh Seo, David O'Donnell, Nimansha Jain, Jason D. Ulrich, Jasmin Herz, Yuhao Li, Mackenzie Lemieux, Jiye Cheng, Hao Hu, Javier R. Serrano, Xin Bao, Emily Franke, Maria Karlsson, Martin Meier, Su Deng, Chandani Desai, Hemraj Dodiya, Janaki Lelwala-Guruge, Scott A. Handley, Jonathan Kipnis, Sangram S. Sisodia, Jeffrey I. Gordon, David M. Holtzman*

INTRODUCTION: Alzheimer's disease (AD) is characterized by early deposition of amyloid- β (A β) plaques followed by pathological tau accumulation. Although A β is a necessary factor in AD pathogenesis, its accumulation in and of itself is insufficient for neurodegeneration and cognitive decline. By contrast, pathological tau accumulation is closely linked with neurodegeneration and cognitive decline in AD and primary tauopathies. Alterations of the gut microbiota have been reported in AD, which

suggests that the microbiota may contribute to AD progression. Animal studies to date have focused mainly on how gut microbiota alterations affect A β pathology and not tauopathy and neurodegeneration. Additionally, recent studies have suggested that apolipoprotein E (ApoE) isoforms, which strongly influence AD risk and regulate tau-mediated neurodegeneration, differentially affect the gut microbiota. Therefore, further investigations to characterize the contribution of the



P301S tau transgenic mice expressing human APOE (TE mice). The dysregulated gut-brain axis and its effect on tauopathy and tau-mediated neurodegeneration. Dysbiosis, unbalanced gut microbiota composition (bottom center), contributes to tau-mediated neurodegeneration by generating bacterial metabolites (e.g., SCFAs) that influence peripheral immune cells. These cells promote central nervous system (CNS) inflammation and contribute to tau aggregation and neurodegeneration. Short-term antibiotics (bottom right) or germ-free conditions (bottom left) reshape or eliminate gut microbiota and reduce their metabolites. These microbiota manipulations influence effects of peripheral immune cells on CNS inflammation and tau-mediated neurodegeneration. ApoE4 in the CNS exacerbates local toxicity and blood-brain barrier dysfunction.

gut microbiota to tauopathy and neurodegeneration are important.

RATIONALE: We assess the hypothesis that the gut microbiota regulates tau pathology and tau-mediated neurodegeneration in an ApoE isoform-dependent manner. A mouse model of tauopathy (*P301S* tau transgenic mice) expressing human ApoE isoforms (ApoE3 and ApoE4), referred to as TE3 and TE4, was subjected to the manipulation of the gut microbiota using two approaches: (i) being raised in germ-free (GF) conditions and (ii) short-term antibiotic (ABX) treatment early in life. Animals were fed a standard mouse chow diet ad libitum until euthanasia at 40 weeks of age, when this mouse model typically has severe brain atrophy.

RESULTS: The gut microbiota manipulations resulted in a notable reduction of tau pathology and neurodegeneration in an ApoE isoform-dependent manner. Both male and female GF TE4 mice showed a marked decrease in brain atrophy compared with conventionally raised (Conv-R) mice. Conv-R ABX-treated TE3 mice had significantly milder hippocampal atrophy compared with controls. ABX-treated TE4 animals showed trends of milder hippocampal atrophy, but the effect did not achieve statistical significance. These phenotypic effects of ABX treatment were not observed in females.

Male GF TE4 mice and male ABX-treated TE3 mice showed significantly lower phosphorylated tau (p-tau) in the hippocampus compared with their controls. Astrocyte and microglial morphology and transcriptomic analysis revealed that the manipulation of the gut microbiota drives glial cells to a more homeostatic-like state, which indicates that gut microbiota strongly influence neuroinflammation and tau-mediated neurodegeneration. Microbiome and metabolite analysis suggests that microbially produced short-chain fatty acids (SCFAs) are mediators of the neuroinflammation-neurodegeneration axis. Supplementation of SCFAs to GF TE4 mice resulted in more reactive glial morphologies and gene expression as well as increased p-tau pathology.

CONCLUSION: The findings reveal mechanistic and translationally relevant interrelationships between the microbiota, the immune response, and tau-mediated neurodegeneration. ApoE-associated gut microbiota targeting may provide an avenue to further explore the prevention or treatment of AD and primary tauopathies. ■

The list of author affiliations is available in the full article online.

*Corresponding author. Email: holtzman@wustl.edu
Cite this article as D. Seo et al., *Science* 379, eadd1236 (2023).
DOI: 10.1126/science.add1236

READ THE FULL ARTICLE AT
<https://doi.org/10.1126/science.add1236>

RESEARCH ARTICLE

NEURODEGENERATION

ApoE isoform- and microbiota-dependent progression of neurodegeneration in a mouse model of tauopathy

Dong-oh Seo¹, David O'Donnell², Nimansha Jain¹, Jason D. Ulrich¹, Jasmin Herz^{3,4}, Yuhao Li⁵, Mackenzie Lemieux^{3,4}, Jiye Cheng², Hao Hu¹, Javier R. Serrano¹, Xin Bao¹, Emily Franke¹, Maria Karlsson², Martin Meier², Su Deng², Chandani Desai², Hemraj Dodiya⁶, Janaki Lelwala-Guruge², Scott A. Handley⁴, Jonathan Kipnis^{3,4}, Sangram S. Sisodia⁶, Jeffrey I. Gordon^{2,4}, David M. Holtzman^{1,7*}

Tau-mediated neurodegeneration is a hallmark of Alzheimer's disease. Primary tauopathies are characterized by pathological tau accumulation and neuronal and synaptic loss. Apolipoprotein E (ApoE)-mediated neuroinflammation is involved in the progression of tau-mediated neurodegeneration, and emerging evidence suggests that the gut microbiota regulates neuroinflammation in an APOE genotype-dependent manner. However, evidence of a causal link between the microbiota and tau-mediated neurodegeneration is lacking. In this study, we characterized a genetically engineered mouse model of tauopathy expressing human ApoE isoforms reared under germ-free conditions or after perturbation of their gut microbiota with antibiotics. Both of these manipulations reduced gliosis, tau pathology, and neurodegeneration in a sex- and ApoE isoform-dependent manner. The findings reveal mechanistic and translationally relevant interrelationships between the microbiota, neuroinflammation, and tau-mediated neurodegeneration.

Alzheimer's disease (AD) is a fatal, progressive neurodegenerative disease, characterized by early deposition of amyloid- β (A β) plaques followed by pathological tau accumulation in the limbic system and neocortex, the latter of which is strongly linked to neuronal loss and brain atrophy (1). Evidence is mounting that there is a link between gut microbiota perturbations and A β deposition, potentially through effects on neuroinflammation and metabolic homeostasis (2–4). However, the contribution of the gut microbiota to tau-mediated neurodegeneration, which is strongly correlated with cognitive decline in AD and other tauopathies, has not been characterized. Furthermore, recent studies have reported that the configuration of the gut microbiota is differentially affected by apolipoprotein E (APOE), the strongest genetic risk factor for AD and a known regulator of tau-mediated neurodegeneration (5, 6). We used a mouse model of tauopathy with animals ex-

pressing different human ApoE isoforms to explore the hypothesis that the gut microbiota regulates tau-mediated neurodegeneration in an ApoE isoform-dependent manner.

TE4 germ-free mice are protected against tau-mediated neurodegeneration

We began by rearing genetically engineered C57BL6J mice containing a *P301S* human tau-expressing transgene and a knocked-in human *APOE4* gene (*Tau/APOE4*, abbreviated TE4) (7) under germ-free (GF) conditions. A second group of TE4 mice was exposed to microbes originating from their TE4 dams beginning at birth; these conventionally raised (Conv-R) mice were subsequently maintained under specified pathogen-free conditions in a mouse barrier facility. A third group of mice was reared under GF conditions until 12 weeks of age, when they received an oral gavage of fecal microbiota sampled from 40-week-old Conv-R TE4 (Ex-GF) mice (Fig. 1A). All mice were given a standard rodent chow rich in plant polysaccharides. We euthanized animals from all groups at 40 weeks of age—a time point when Conv-R TE4 mice display substantially greater tau-mediated neurodegeneration compared with (i) Conv-R P301S mice harboring other human APOE isoforms in their genomes or (ii) Conv-R animals lacking both mouse and human APOE (7, 8). Unless otherwise indicated, all analyses were performed using biospecimens obtained from 40-week-old mice.

Conv-R male and female TE4 mice displayed severe regional brain atrophy, manifested by

hippocampal volume loss and lateral ventricle (LV) enlargement relative to E4 mice lacking the tau transgene (Fig. 1, B and D). However, GF male and female TE4 mice had significant preservation of brain tissue compared with their Conv-R TE4 counterparts, as judged by hippocampal and LV sizes as well as by measurements of hippocampal neuronal layer thickness—a direct estimate of neuronal loss (fig. S1, C and D). Comparison of these areas of the brain in 12- and 40-week-old TE4 mice provided evidence that the protective effect produced by the GF state reflected a blockade of progression of neurodegeneration (fig. S1, E and F). We did not detect rescue from neurodegeneration in the entorhinal-piriform cortex of GF TE4 animals (fig. S1G).

The GF rescue from neurodegeneration was reversed when animals were colonized with fecal microbial communities harvested from sex-matched Conv-R TE4 animals (fig. S1, H to J); 28 weeks after colonization, 40-week-old Ex-GF mice exhibited hippocampal and LV volumes and hippocampal neuronal layer thicknesses comparable to those documented in Conv-R mice (Fig. 1, B and D, and fig. S1D). Staining brain sections with a phospho-tau antibody (AT8) revealed a marked decrease in tau phosphorylation in 40-week-old GF compared with 40-week-old Conv-R mice (Fig. 1, C and E). By contrast, we did not observe any differences in hippocampal AT8 staining between 12-week-old GF and 12-week-old Conv-R mice (fig. S1, K and L). Thus, the microbiota greatly affects the later appearance of tau-mediated neurodegeneration.

TE4 GF mice exhibit reduced reactive gliosis

Although elevated levels of pathological phosphorylated tau (p-tau) may directly contribute to neuronal degeneration and death, there is strong evidence that reactive microglia and astrocytes are required for tau-mediated neurodegeneration (7, 9–11). Recent studies have indicated that the gut microbiota contribute to glial functions (12–14), leading us to hypothesize that the microbiota may modulate tau-mediated neurodegeneration in our model by altering glial reactivity. Therefore, we first stained brain sections with markers for astrocytes and microglia [glial fibrillary acidic protein (GFAP), Iba1, and CD68]. Consistent with the amount of degeneration, expression of all these glial markers in the hippocampus was strongly reduced in GF compared with Conv-R male mice (Fig. 2, A and B). Furthermore, analysis of glial morphology in the hippocampus (fig. S2, A to D) revealed that astrocytes in GF mice were larger with more branched processes compared with those in Conv-R mice. These morphological alterations of glial cells in GF mice were also observed at 12 weeks of age, when there is mild p-tau

¹Department of Neurology, Hope Center for Neurological Disorders, Washington University School of Medicine, St. Louis, MO, USA. ²The Edison Family Center for Genome Sciences and Systems Biology and the Center for Gut Microbiome and Nutrition Research, Washington University School of Medicine, St. Louis, MO, USA. ³Center for Brain Immunology and Glia (BIG), Washington University School of Medicine, St. Louis, MO, USA. ⁴Department of Pathology and Immunology, Washington University School of Medicine, St. Louis, MO, USA. ⁵Division of Infectious Diseases, Department of Medicine, Washington University School of Medicine, St. Louis, MO, USA. ⁶Department of Neurobiology, The University of Chicago, Chicago, IL, USA. ⁷Knight Alzheimer Disease Research Center, Washington University School of Medicine, St. Louis, MO, USA.

*Corresponding author. Email: holtzman@wustl.edu

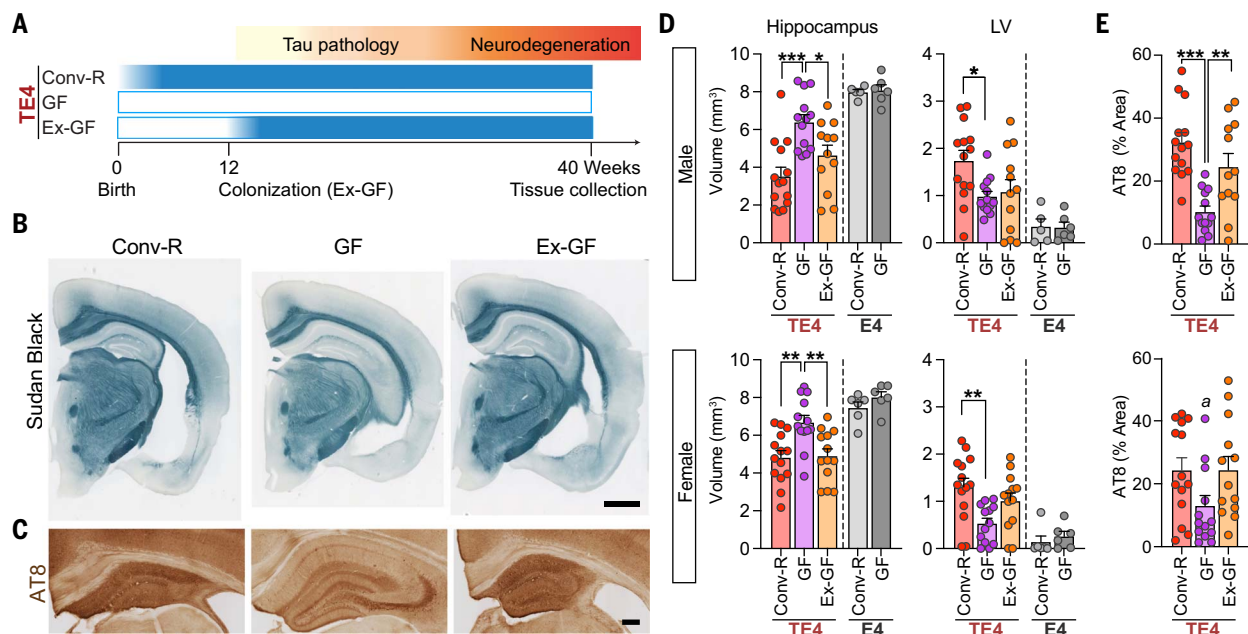


Fig. 1. TE4 GF mice are protected against tau-mediated neurodegeneration.

(A) Experimental design. TE4 mice were reared in a vivarium in a specified pathogen-free state (Conv-R; $n = 14$ per sex) or under GF conditions in gnotobiotic isolators (GF; $n = 13$ to 14 per sex) until they were euthanized at 40 weeks of age. A separate group of 12-week-old GF mice were colonized with fecal microbiota harvested from sex-matched 40-week-old Ex-GF mice ($n = 12$ per sex). (B) Representative images of 40-week-old male Conv-R, GF, and Ex-GF mouse brain sections stained with Sudan black. Scale bar, 1 mm. (C) Representative images of p-tau staining (AT8) in the hippocampus of male mice. Scale bar, 250 μ m.

(D) Volumes of the hippocampus (left) and LVs (right) in male (top) and female (bottom) mice. E4 represents APOE4 knock-in mice that lack a P301S tau transgene. (E) Percentage area covered by AT8 staining in sections prepared from the hippocampus of 40-week-old male (top) and female (bottom) TE4 mice. Data are presented as mean values \pm SEMs. Statistical significance was defined using a one-way ANOVA with Tukey's post hoc test. * $P < 0.05$; ** $P < 0.01$; *** $P < 0.001$. The letter "a" in (E) indicates that, in the post hoc analysis, Tukey did not reveal significant differences, but least significant difference (LSD) showed $P < 0.05$ (GF versus Conv-R and Ex-GF). See table S1 for full statistical results.

pathology but no evidence for neurodegeneration (fig. S3).

Analysis of differential gene expression using nCounter (NanoString Technologies) showed that at 40 weeks of age, the GF state was associated with down-regulation of genes related to innate immune responses (including *sox9* and *cx3cr1*), apoptosis, and autophagy and up-regulation of genes related to neuronal activity and epigenetics (fig. S4A and data S2). No significant differences in gene expression were detected when comparing Conv-R with Ex-GF mice (data S3). Weighted gene coexpression network analysis using the Nanostring data identified five coexpression modules, two of which (modules Grey and Turquoise) exhibited significant correlation with either microbial colonization status or hippocampal size (fig. S4, B to D). Gene ontology (GO) analysis demonstrated that module Grey was enriched for genes related to epigenetics, T cell-mediated immunity (e.g., *Foxp3*, which is associated with regulatory T cells), and gliogenesis (e.g., *Tmem119*, which is typically up-regulated in homeostatic microglia). Module Turquoise was enriched for genes related to cytokine production, cell death, and defense response, including *APOE* (fig. S4, E and F, and data S4). Analysis of eigengene (the first principal component of the

expression matrix of the corresponding module) expression in modules Grey and Turquoise by individual animal verified that increased and decreased expression, respectively, in these modules were tightly linked to the protective effect of the GF condition (fig. S4, G to J). Thus, GF conditions affect microglia and astrocyte reactivity or activation associated with tau-mediated neurodegeneration.

Antibiotic-induced gut microbiota perturbation protects against tau-mediated neurodegeneration

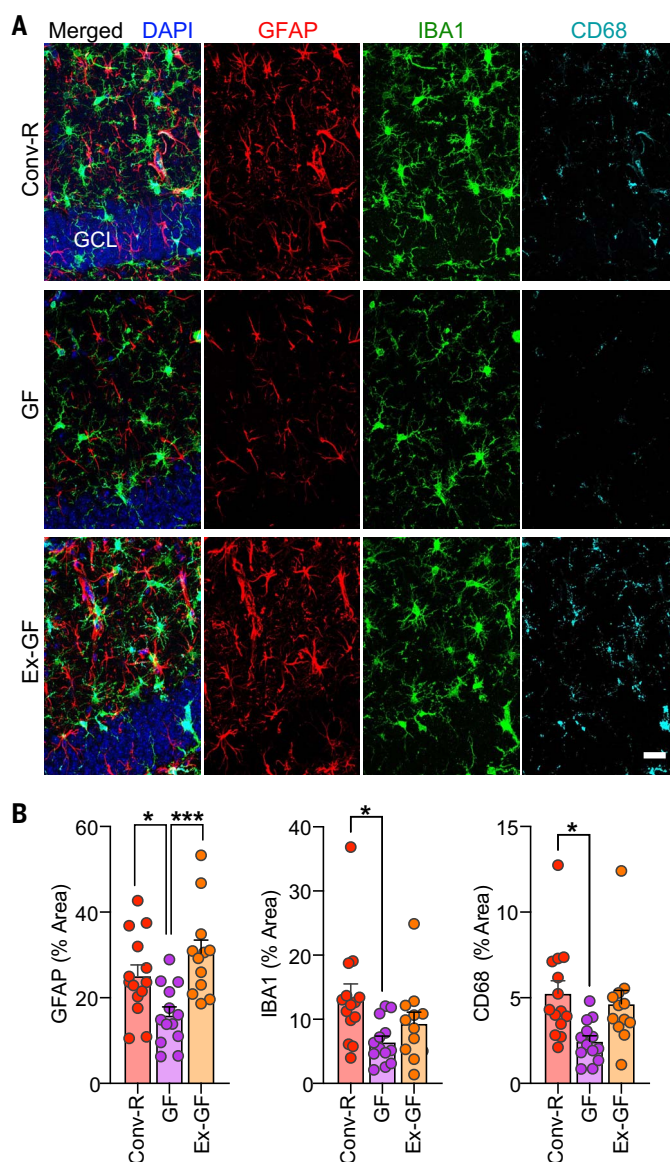
To test whether the gut microbiota regulates tau-mediated neurodegeneration in an ApoE isoform-dependent manner, we treated groups of Conv-R TE4 mice, P301S tau transgenic mice expressing human APOE3 (TE3), and P301S tau animals without APOE (TEKO) with an antibiotic cocktail (ABX) composed of kanamycin, gentamicin, colistin, metronidazole, and vancomycin (4). Gavage with the antibiotic cocktail (or water in the case of controls) occurred daily from postnatal days 16 to 22. The fecal microbiota was serially sampled, and animals were euthanized at 40 weeks of age (Fig. 3A). The short-term ABX treatment produced a marked, immediate decrease in the total number of viable bacteria; although this

decrease in viability was transient, culture-independent methods disclosed that the proportional representation of various bacterial taxa in the microbiota of ABX-treated groups remained different from controls throughout life (see fig. S5, A to E, and below).

Volumetric analysis revealed that 40-week-old male mice in the H₂O-treated control groups (TE3-H₂O and TE4-H₂O animals) had statistically significant hippocampal atrophy compared with mice lacking the APOE gene (TEKO) (Fig. 3, B and C) (8). However, TE3-ABX but not TE4-ABX mice showed significant hippocampal preservation relative to controls. Enlargement of the LV and entorhinal-piriform cortical atrophy were also significantly attenuated by ABX treatment independent of APOE genotype, but the degree of ABX effect was higher in TE3 compared with TE4 mice in general (i.e., the log₂ fold changes by ABX in the LV size were -0.86 in TE3 and -0.34 in TE4 mice; the log₂ fold changes by ABX in the entorhinal-piriform cortex size were 0.57 in TE3 and 0.36 in TE4 mice; Fig. 3C and fig. S5F). ABX treatment also prevented thinning of hippocampal neuronal cell layers independent of APOE genotype (fig. S5G). These phenotypic effects of ABX treatment were seen in TE3 and TE4 males but not in females,

Fig. 2. TE4 GF mice exhibit reduced reactive gliosis.

(A) Representative immunofluorescence images of hippocampal sections from 40-week-old male Conv-R, GF, and Ex-GF mice stained with antibodies to GFAP (red), Iba-1 (green), and CD68 (cyan) as well as DAPI (blue). Scale bar, 25 μ m. GCL, granule cell layer. (B) Percent of the area of sections taken from the hippocampus covered by GFAP (left), Iba-1 (middle), and CD68 (right) staining. Mean values \pm SEMs are shown ($n = 12$ to 14 per group). Statistical significance was defined by one-way ANOVA with Tukey's post hoc test. * $P < 0.05$; *** $P < 0.001$. See table S1 for full statistical results.



except in the case of the CA1 pyramidal layer, which was slightly, albeit significantly, thicker in ABX-treated males and females (fig. S5G). In concert with hippocampal brain atrophy, male TE3-ABX mice showed significantly lower AT8 staining relative to male TE3-H₂O mice (Fig. 3, D and E).

ABX treatment did not influence brain volume or early tau pathology in 12-week-old male TE3 mice (fig. S5, H to K). At 40 weeks of age, analysis of male cortical tissue also revealed that ABX treatment reduced p-tau levels in the detergent-soluble fraction (RIPA) and both p-tau and human tau levels in the insoluble fraction (FA) across the three APOE genotype groups (fig. S6). Furthermore, nest-building behaviors, known to be sensitive to hippocampus damage and neurodegenerative disease (15), showed significant improvement in male TE3 and TE4 mice treated with ABX,

which correlated with hippocampal volumes (fig. S7).

Antibiotic treatment alters astrocyte and microglial gene expression and morphological responses

Single-nucleus RNA sequencing (snRNA-seq) of hippocampal tissue collected from Conv-R 40-week-old males that belonged to all three APOE genotype groups and were not exposed to antibiotics identified 20 distinct clusters, which were categorized into excitatory and inhibitory neurons, astrocytes, microglia, oligodendrocytes, and oligodendrocyte progenitor cells (fig. S8, A and B). Cell proportion analysis showed that certain neuronal populations (e.g., exc1, exc2, and exc5) were reduced in the presence of tau pathology and expanded again with ABX treatment, in agreement with the hippocampal volumetric data. The astrocyte population was reduced twofold with ABX in the

presence of tau pathology. The microglial population, which expanded approximately sevenfold (by proportion) with tau pathology, was reduced two- to threefold with ABX treatment.

The astrocyte cluster was rescaled and re-clustered, revealing four subclusters (astro0 to astro3; Fig. 4A and fig. S8C). Reclustering of the microglia cluster identified three subclusters (micro0 to micro2; Fig. 4H and fig. S8D). Tau pathology resulted in a strong shift from astro0 to astro1 and micro0 to micro1. ABX treatment reversed these shifts in TE3 but not TE4 male mice, consistent with a stronger protective effect with ABX treatment in TE3 compared with TE4 male mice. Further differentially expressed gene (DEG) analysis between two clusters associated with pathological shifts revealed that the top up-regulated pathways in astrocyte subcluster DEG (astro1 versus astro0; data S5) were associated with GO terms related to gliogenesis and cellular chemical homeostasis (Fig. 4B), whereas the top up-regulated pathways in the microglial subcluster DEG (micro1 versus micro0; data S6) were associated with GO terms related to cell activation and small guanosine triphosphatase (GTPase)-mediated signal transduction (Fig. 4I). We used quantitative polymerase chain reaction (qPCR) to verify up-regulation of a subset of astro1 genes (e.g., *Gfap* and *Vim*) and micro1 genes (e.g., *Arhgap25* and *Itgax*) (fig. S9, A and B). An alteration of glial gene expression was also observed in ABX-treated TE3 mice at 12 weeks of age, well before neurodegeneration (fig. S9C). Thus, the gut microbiota regulates expression of genes that are involved in reactive gliosis.

Reactive gliosis is a complex process that involves changes in gene expression and morphological remodeling. In general, homeostatic glial cells display highly branched thin processes in the homeostatic state, but in activated cells, processes become shorter as they retract and become hypertrophic (16). To further assess reactive gliosis, we performed GFAP, Iba1, and CD68 immunostaining. Although the coverage area of the immunostaining did not reveal significant ABX effects (fig. S10A), morphometric analysis revealed that ABX drove astrocytes and microglia to a more homeostatic-like morphological state (e.g., increased length of processes and size of cells) in male TE3 mice but not in male TE4 and TEKO, female TE3, or male 12-week-old TE3 mice (Fig. 4, C to G and J to L, and fig. S10, B to K). Thus, ABX-induced perturbation of the microbiota protects against tau-mediated neurodegeneration most strongly in male TE3 mice, and this effect is manifested by changes in multiple cell types, including astrocytes and microglia.

Antibiotic treatment reshapes the bacterial communities and reduces short-chain fatty acids

The microbiota perturbation induced by ABX was evidenced by (i) measurements of cecal

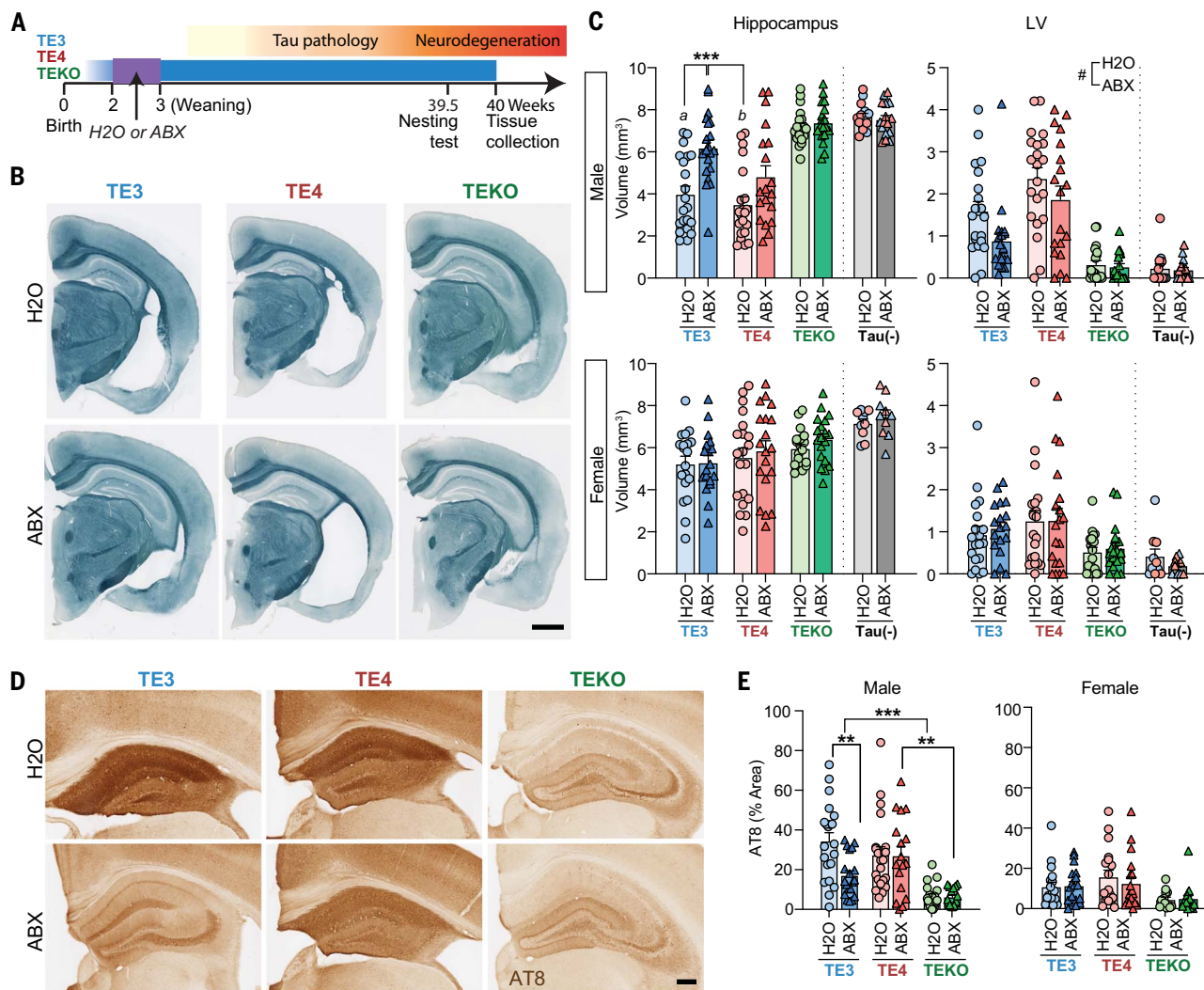


Fig. 3. Antibiotic treatment and perturbation of the gut microbiota markedly protects against tau-mediated neurodegeneration in a sex- and ApoE isoform-dependent manner. (A) Male and female TE3, TE4, and TEKO transgenic mice ($n = 18$ to 21 per group) received a gastric gavage of a combination of antibiotics (ABX) from postnatal days 16 to 22. Controls were gavaged with water (H₂O). Mice were euthanized at 40 weeks of age. (B) Representative images of male TE3, TE4, and TEKO mouse brain sections stained with Sudan black. Scale bar, 1 mm. (C) Volumes of the hippocampus (left) and LVs (right) in male (top) and female (bottom) animals. Tau(-) represents APOE3 (blue) or APOE4 (red) knock-in mice that lack a P301S tau

transgene. (D) Representative images of p-tau staining (AT8) of hippocampal sections prepared from male mice. Scale bar, 250 μm. (E) Percentage of the area covered by AT8 staining of hippocampal sections prepared from male (left) and female (right) mice. Mean values ± SEMs are shown. Statistical significance defined by two-way ANOVA with Tukey's post hoc test. * $P < 0.05$; ** $P < 0.01$; *** $P < 0.001$. Statistical significance of the main effects of treatments (H₂O versus ABX) were indicated as # $P < 0.05$. In (C) (male hippocampus), *a* indicates statistical significance compared with TEKO-H₂O and TEKO-ABX groups ($P < 0.001$), and *b* indicates statistical significance compared with TE3-ABX, TEKO-H₂O, and TEKO-ABX ($P < 0.001$). See table S1 for full statistical results.

weight compared with body weight (known to be markedly increased in GF compared with Conv-R animals and rapidly reduced in Ex-GF mice; fig. S1, A and B, and fig. S5, D and E) and (ii) culture-independent analysis of the relative abundances of bacterial taxa in feces. The latter approach was based on sequencing PCR amplicons generated from variable region 4 of bacterial 16S ribosomal RNA (rRNA) genes [amplicon sequence variants (ASVs)] and grouping these ASVs into taxonomic bins. Alterations in alpha and beta diversity as well

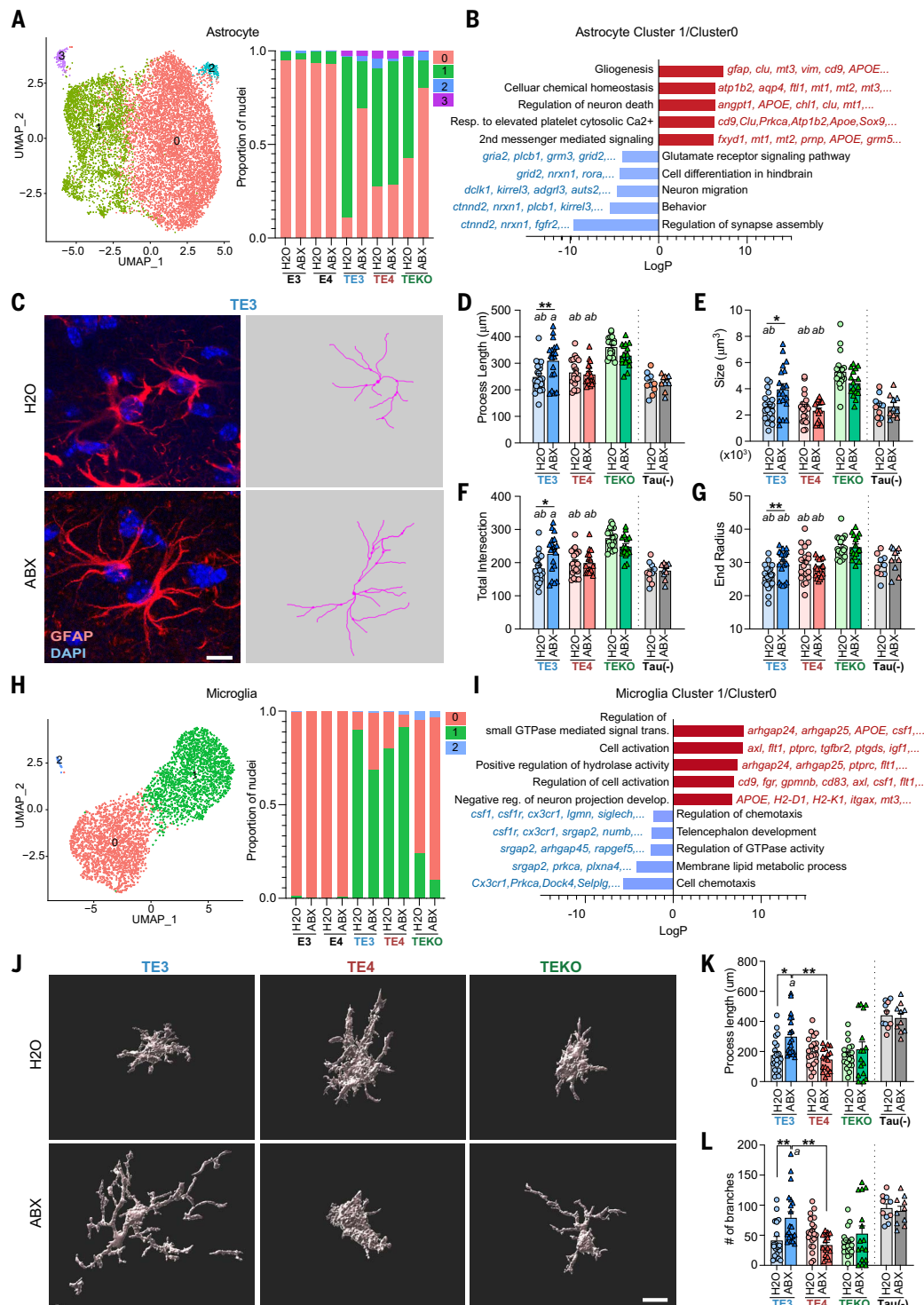
as the representation of phylum- and genus-level groups are summarized in figs. S11 to S13. Phylum- and genus-level changes in ABX-treated groups remained different from H₂O-treated controls up to the time of euthanasia (fig. S11, D and E).

Linear discriminant analysis revealed that the members of the genera *Helicobacter*, *Ruminococcus*, and *Butyrivibrio* had lower relative abundance in the fecal microbiota of ABX-treated groups across male APOE isoform groups (Fig. 5A and fig. S12, A to C) but not in female TE3

mice (Fig. 5B and fig. S13D). Recent studies have suggested that the microbiota modulates glial activation through the production of microbial metabolites, such as short-chain fatty acids (SCFAs) (12, 13). *Ruminococcus* and *Butyrivibrio* are associated with SCFA production. Also, the relative abundance of several bacterial family-level taxa known to produce SCFAs, such as *Ruminococcaceae* and *Lachnospiraceae*, were reduced with ABX across APOE genotypes (fig. S12D). The representation of these taxa was greater in male compared with

Fig. 4. Glial transcriptional and morphological responses to tau pathology are regulated by ABX treatment.

(A) (Left) UMAP plot of a reclustered astrocyte population that identifies four distinguishable clusters (astrocyte cluster 0 to 3). (Right) Relative frequency of all astrocyte clusters per genotype and treatment. (B) GO biological process terms significantly enriched among DEGs (astrocyte cluster 1 versus 0). (C) (Left) Representative images of male TE3 mouse brain sections stained with GFAP and DAPI. (Right) Traces of GFAP expression generated using Simple Neurite Tracer, corresponding to the images on the left. Scale bar, 10 μ m. (D to G) Morphometric analysis of astrocyte process lengths (D), size of GFAP+ astrocytes (from Convex Hull analysis) (E), total number of process intersections (F), and the end radius (from Sholl analysis) (G). (H) (Left) UMAP plot of the reclustered microglial population showing three distinguishable clusters (microglia clusters 0, 1, and 2). (Right) Relative frequency (proportion of nuclei) of all microglia clusters per genotype and treatment group. (I) GO terms enriched in up-regulated and down-regulated DEGs (microglia cluster 1 versus 0). (J) Imaris-based automatic reconstruction image of Iba1+ microglia. Scale bar, 10 μ m. (K and L) Morphometric analysis of process lengths (K) and the number of branches (L) of Iba1+ microglial cells in male TE3, TE4, and TEKO mice. Tau(-) represents APOE3 (blue) or APOE4 (red) knock-in mice that lack a P301S transgene. Mean values \pm SEMs are presented with statistical significance defined by two-way ANOVA with Tukey's post hoc test. * P < 0.05; ** P < 0.01; *** P < 0.001. *a* and *b* indicate statistical significance compared with TEKO-H₂O (*a*) and TEKO-ABX (*b*) (P < 0.05). See table S1 for full statistical results.



female members of the TE3-H₂O treatment group (Fig. 5C) and lower in TE3 compared with TE4 mice (fig. S13, B and C). Gas chromatography-mass spectrometry (GC-MS) of cecal samples disclosed that, consistent with our observation that SCFA-producing bacteria were reduced with ABX treatment in males, acetate, propionate, and butyrate were significantly reduced across APOE genotypes in males, cor-

relating with biomarkers of tau pathology (Fig. 5, D and E, and fig. S13A), but not in females (fig. S13E).

ABX-induced gut microbiota perturbation alters the peripheral immune system and the effects of SCFA on TE4 GF mice

It is unclear whether SCFAs act directly on glial cells because SCFA receptor-encoding

genes (e.g., *Ffar2*) are not expressed in glial cells (12). However, we postulated that SCFAs could affect other inflammatory mediators or immune cells that directly access the brain (i.e., the meninges). We found reductions in meningeal natural killer (NK) and plasmacytoid dendritic cells (pDC) cells in ABX-treated TE3 mice. Furthermore, $\gamma\delta$ T and pDC cells were reduced

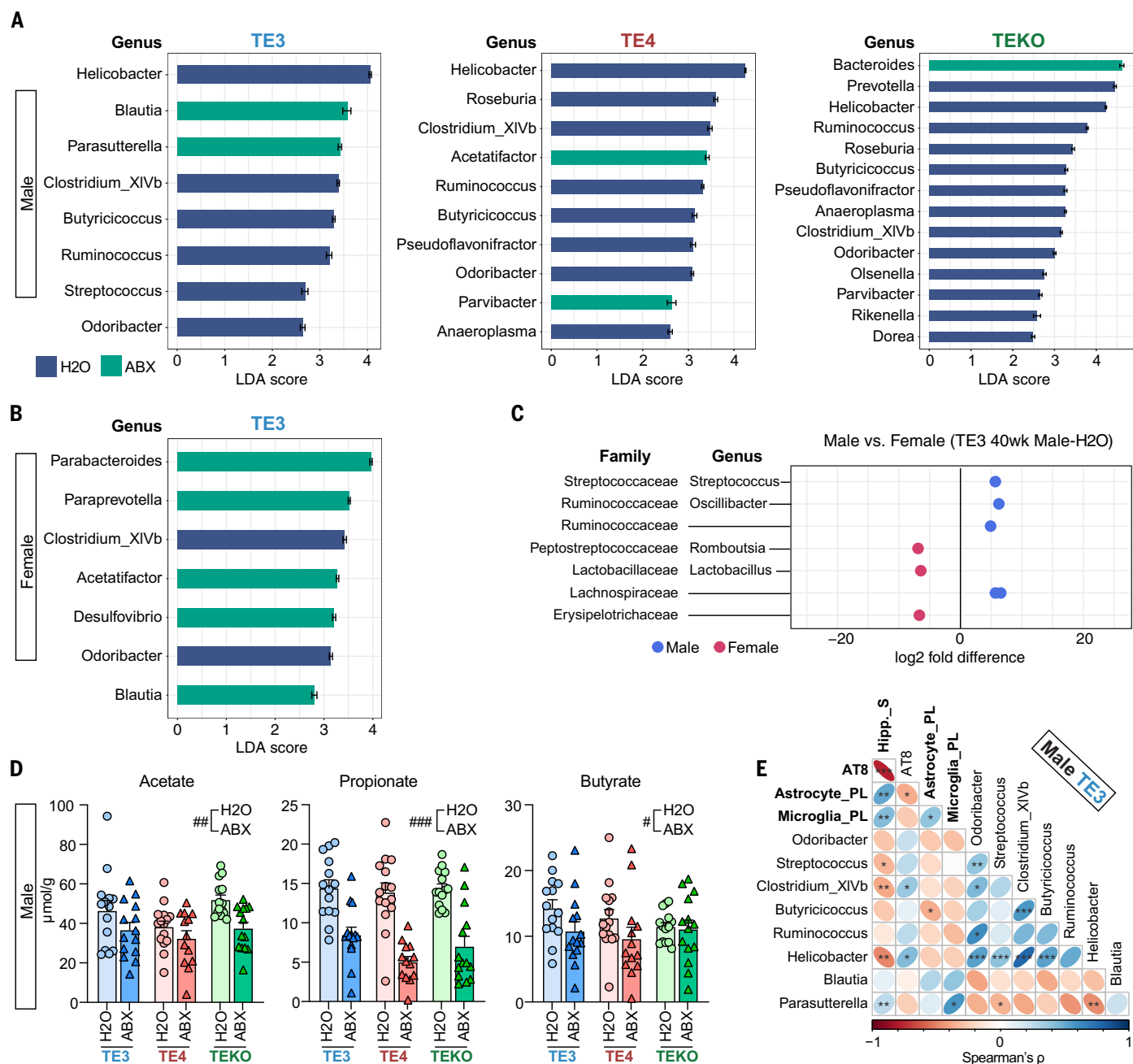


Fig. 5. Effects of ABX treatment on fecal microbiota composition and cecal levels of SCFAs. (A and B) Linear discriminant analysis (LDA) scores. Horizontal bars represent the LDA scores for each genus-level taxon in male TE3, TE4, and TEKO mice (A) and in female TE3 mice (B). Indigo and green bars represent taxon features with significantly higher representation in mice belonging to the control H₂O and versus ABX treatment groups, respectively (LDA scores > 2). (C) Comparison of relative abundance of genera between 40-week-old male and female TE3-H₂O mice. Family and genus assignments are shown. (D) Targeted GC-MS analysis of cecal SCFAs in male 40-week-old TE3, TE4, and TEKO mice treated with ABX or H₂O ($n = 14$ per group), tested by

two-way ANOVA. Statistical significance of the main effects of treatments (H₂O versus ABX) were indicated as # $P < 0.05$, ## $P < 0.01$, and ### $P < 0.001$. (E) Correlogram showing the relationship between (i) eight genera identified as having differences in their relative abundance in male 40-week-old TE3 H₂O- versus ABX-treated mice and (ii) biomarkers of tauopathy. These biomarkers (bold) include hippocampus size (Hipp_S; smaller value reflecting greater neurodegeneration), coverage of AT8 staining, process length of astrocytes (astrocyte_PL), and process length of microglial cells (microglia_PL). * $P < 0.05$; ** $P < 0.01$; *** $P < 0.001$. See table S1 for full statistical results.

in GF mice (fig. S14, A to C). These latter cells are known to release cytokines, such as interleukin-17 (IL-17), interferon (IFN) type-I, and others, which may affect neuroinflammation in the brain (17–19).

Multiplex cytokine profiling revealed that plasma levels of MCP-3, IL-2R, BAFF, and Eotaxin were significantly reduced by ABX in mice (fig. S15). The degree of reduction of Eotaxin, which can cross the blood-brain bar-

rier and activate glial cells, was greater in TE3 mice compared with those belonging to the other genotype groups. Gut microbiota can modulate systemic immunity, including peripheral macrophages (20). ABX treatment of

male TE3 mice significantly altered lung alveolar macrophage gene expression (fig. S16). In turn, their cytokine release or interaction with adaptive immune cells could potentially affect brain pathology. The cytokine profiling data showed that some cytokines released by macrophages, such as IP-10 and BAFF, or those that can stimulate macrophages, such as MIP-1 α , were affected by ABX treatment. Brain border innate and infiltration of peripheral immune cells also may act on the tau pathology and neurodegeneration. Additional snRNA-seq analysis using hippocampal tissue revealed that the populations of brain border and peripheral immune cells were increased in the tau mice at 40 weeks of age and were decreased by ABX treatment (fig. S14D). Although changes in peripheral cytokines may be important to activate glial cells to drive tau-mediated neurodegeneration, the presence of ApoE in the brain is still necessary to drive tau-mediated neurodegeneration because these cytokines in the plasma display high levels in TEKO mice that only display mild brain atrophy (Fig. 3C and fig. S15B). Finally, to begin to test whether SCFAs may be mediating the effects of GF conditions or ABX, we administered SCFAs or control in drinking water to 10-week-old or 31-week-old TE4 GF mice for 5 or 4 weeks, respectively. SCFA treatment altered alveolar macrophage gene expression in both the younger and older mice (fig. S17). SCFA supplementation increased gliosis and p-tau pathology in the hippocampus of the older TE4 GF mice (fig. S18), supporting the possibility that SCFA may be a key modulator of the microbiota effect on tau-mediated neurodegeneration.

Conclusion

Taken together, we have found that GF conditions are strongly neuroprotective against tau-mediated neurodegeneration in male and female TE4 mice. ABX treatment is also neuroprotective, but its effect was limited to males and was greater in the presence of APOE3 compared with APOE4. Our results also suggest that APOE isoforms and sex differentially modulate the microbial response to ABX, resulting in significantly lower levels of SCFAs. The microbiota-associated metabolic changes are associated with altered peripheral cytokine responses and strong changes in the innate immune response in the brain.

We hypothesize that the gut microbiota regulates the brain's innate immune response to influence tau-mediated neurodegeneration in the brain. We speculate that in TE3 mice, the ABX-induced microbiota perturbation that reduces peripheral immune activation may moderate the brain's innate immune response and eventually attenuate tau-mediated neurodegeneration. By contrast, in TE4 mice, the microbiota-associated peripheral immune changes were not altered as much by ABX treat-

ment. It is possible that the gain of function of APOE4 toxicity and the effects on the local innate immune response in the brain were stronger than that of APOE3, and ABX treatment ultimately failed to protect against tau-mediated neurodegeneration to the same degree. On the other hand, with the complete absence of the microbiota, even in TE4 mice, the depletion of microbially produced metabolic and immune signals results in a strong reduction of the disease-associated astrocyte and microglial phenotypes, leading to a decrease in tau-mediated neurodegeneration (consistently, SCFA supplementation reversed the reduced gliosis and tau pathology in TE4 GF mice).

Further studies are needed to test these hypotheses and to gain greater understanding of how sex, microbiota manipulation, microbiota-linked metabolites, central or peripheral immune response, and the pathogenesis of neurodegeneration are related. A starting point for these follow-up analyses could involve gnotobiotic mice colonized with gut microbiota harvested from Conv-R mice with different sex, age, and ApoE isoforms and from human donors (with or without tau-mediated neurodegeneration). It is possible that the TE4 GF mice colonized with different types of microbiota (e.g., harvested from wild-type mice, not necessarily from TE4-Conv-R mice) would reverse the GF rescue from neurodegeneration. It may be that the host genetic makeup in TE4 mice could reshape the effects of the transferred microbiota composition derived from a more general bacterial community and be sufficient to activate the metabolic-neuroinflammation axis. Alternatively, the sex, age, ApoE isoform status, and state of neurodegeneration may be critical in regard to the source from which the transferred microbiota are derived. Future studies are needed to sort out these possibilities. Nonetheless, these results raise the possibility that gut microbiota targeting may provide ways to prevent or treat progression of AD and primary tauopathies (21, 22).

Materials and methods

Animals

All animal experiments were performed using protocols approved by the Institutional Animal Care and Use Committee (IACUC) at Washington University School of Medicine. All phenotyping and data analyses were performed by researchers who were completely blind to the experimental hypothesis and the treatments of mice.

P301S tau transgenic mice (PS19tg; Stock No. 008169, Jackson Laboratories) contain a transgene, where expression of the human P301S tau mutant is driven by a mouse prion protein (Prnp) promoter. These animals had been backcrossed to C57BL/6 mice (Stock No.

027, Charles River) for more than 10 generations. P301S mice were crossed with human APOE knock-in mice, where the endogenous mouse ApoE gene was replaced by a human APOE gene flanked by LoxP sites (23) (APOE3^{fllox/fllox} or APOE4^{fllox/fllox} or ApoE knockout mice) to generate P301S::APOE3/wt, APOE4/wt, or EKO/wt animals [wild-type (wt)]. These mice were then crossed to homozygous APOE3, APOE4, or EKO mice to generate P301S::ApoE3/ApoE3, ApoE4/ApoE4, or EKO/EKO mice (abbreviated as TE3, TE4, and TEKO, respectively). Sires and dams were randomly assigned from different litters to produce experimental animals. Dams that had received an antibiotic cocktail (see below) were euthanized after weaning their pups on postnatal day 23 and were not used for further breeding or any other experiments. At weaning (postnatal day 23), pups were housed in same-sex, -genotype, and -treatment groups (2 to 5 animals per cage). Conv-R mice were housed in a mouse barrier facility under specified pathogen-free conditions until they were euthanized at 40 weeks of age. All Conv-R mice in the antibiotic experiment were given the same type of food (no. 53WU, LabDiet, St. Louis, MO) ad libitum. All groups of animals were housed under the same conditions: same type of cage, bedding materials (no. Bed-o'Cobs 1/8 BB40; the Andersons, Quakertown, PA), and nestlets (no. NES7200; Ancare, Bellmore, NY) in the same room in the vivarium. A complete mouse cage consisted of a polycarbonate shoebox bottom equipped with a wire bar lid and a polycarbonate filter top containing a filter insert.

Conv-R TE4 mice were rederived as GF by embryo transfer. Embryos were harvested 1 day after mating and transferred under sterile conditions to a pseudopregnant GF mother generated by mating to a vasectomized GF male. The transgenic GF descendants were intercrossed to produce TE4 GF mice. GF animals were reared in plastic flexible film gnotobiotic isolators (Class Biologically Clean Ltd., Madison, WI). GF status was verified by PCR of feces using universal bacterial 16S rRNA gene primers and by culturing fecal and skin swabs. The equivalent generation of Conv-R mice were used as controls.

GF mice were colonized with fecal microbiota samples collected from 40-week-old Conv-R TE4 mice to create Ex-GF animals. To do so, fecal samples from 4 to 5 mice per sex were pooled, homogenized in sterile reduced phosphate-buffered saline (PBS) containing 0.05% cysteine-HCL and 20% glycerol (5 pellets/10 mL) and stored in -80°C until the time of the fecal microbiota transplantation. A 200- μL aliquot of the resulting suspension was thawed and administered to sex-matched 12-week-old GF mice by oral gavage on two occasions, separated by a 4-day interval. The Ex-GF mice were maintained in plastic flexible

film gnotobiotic isolators (Class Biologically Clean Ltd., Madison, WI) (2 to 5 mice of the same sex per cage).

All Conv-R, GF, and Ex-GF mice (2 to 5 mice of the same sex per cage) were given the same type of autoclaved food (Teklab certified global 18% protein rodent diet; catalog no. T2018SC.15) ad libitum. All animals were maintained under a strict light cycle (lights on at 0600 hours and off at 1800 hours). Fresh fecal pellets from each animal were collected directly in sterile 2-mL centrifuge tubes (Axygen; SCT-200-SS-R-S) and immediately stored in -80°C until the time of DNA extraction. All fecal pellet samples were collected at between 1500 hours and 1700 hours to minimize circadian rhythm effects.

Antibiotic treatment

Pups assigned to the ABX treatment group were gavaged with 100 μL of an antibiotic cocktail that contained 4 mg/mL kanamycin (Sigma-Aldrich K4000), 0.35 mg/mL gentamicin (Sigma-Aldrich G1914); 8500 U/mL colistin (Sigma-Aldrich C4461), 2.15 mg/mL metronidazole (Sigma-Aldrich M1547), and 0.45 mg/mL vancomycin (Sigma-Aldrich V2002) (prepared using autoclaved water). Gavage occurred daily from postnatal day 16 to 22 using animal feeding needles (Cadence; catalog no. 7901). Control mice were gavaged with 100 μL of water (4, 24). After each gavage, mice were transferred to a new sterile cage to avoid contamination from accumulated feces in the old cages.

Nest-building behavior

A few days before euthanasia, group-housed mice were switched to individual housing (7, 25). Preweighed nestlets (2.5 g; no. NES7200, Ancare, Bellmore, NY) were introduced into each cage at ~ 1600 hours. The next morning at 1000 hours, the remaining nestlet was weighed. A 5-point scale was used to score the results; the scoring system is based on the percentage of nesting material remaining plus the shredding conditions: score = 1, nest shredding $<25\%$; 2, nest shredding 25 to 50%; 3, nest shredding 50 to 90%; 4, nest shredding $>90\%$, but nest was not compacted yet; 5, complete nest built (fig. S7A).

Tissue collection

Mice received a lethal intraperitoneal injection of pentobarbital (200 mg/kg). After perfusion with a solution of cold Dulbecco's PBS containing 3 U/ml heparin, the brains were removed. The left hemisphere was fixed in 4% paraformaldehyde for 24 hours before being transferred to 30% sucrose and stored at 4°C until sectioning. Brains were cut coronally into 50- μm -thick sections on a freezing sliding microtome (Leica SM1020R) and stored in cryoprotectant solution (0.2 M PBS, 15%

sucrose, 33% ethylene glycol) at -20°C until use. Right hemispheres were dissected, flash-frozen on dry ice, and stored at -80°C for biochemical analyses.

Volumetric analysis

Volumetric analysis of the hippocampus, LV, and entorhinal-piriform (Ent-Piri) cortex was performed using a stereological method that involved assessing every sixth coronal brain section (300 μm between sections), starting rostrally from bregma -1.4 mm to bregma -3.1 mm. All sections from each mouse were mounted on a glass slide. All mounted sections were completely dried, rinsed in water for 1 min, and stained with 0.1% Sudan black in 70% ethanol at room temperature for 20 min, then washed in 70% ethanol for 1 min (three times). Sections were then washed in Milli-Q water three times and cover-slipped with Fluoromount. The stained sections were imaged with a NanoZoomer microscope (Hamamatsu); areas of interest were traced and measured in each section using the NDP viewer (Hamamatsu). Volume was calculated by the sum of area \times 0.3 mm (7, 8). All staining and analysis of data obtained were performed by someone who was blind to the experimental hypothesis and the treatments of the animals being assessed.

Neuronal layer thickness measurement

Left hemi-brain sections from each mouse, corresponding approximately to bregma coordinates -1.7 and -2.7 mm, were mounted and stained in cresyl violet for 5 min at room temperature (7). Slices were sequentially dehydrated in 50%, 70%, 95% (three times), and 100% ethanol (twice) (1 min per treatment) then cleared in xylene for 4 min (twice), and cover-slipped in cytochrome 60 (Thermo Fisher Scientific, catalog no. 8310-16). Images were taken using Cytation 5 (Biotek) and analyzed with Gen5 Software (Biotek). Quantification of the thickness of the dentate granular cell layer and the CA1 pyramidal layer were measured by drawing a scale line that crossed the cell layers at two areas each section and obtaining the average value. All staining and analysis of data obtained were performed by individuals blind to the experimental hypothesis and the treatments of the animals being assessed.

Immunohistochemistry

Left hemi-brain sections, corresponding approximately to bregma coordinates -1.5 and -1.8 mm, were used for immunohistochemistry. For AT8 staining, brain sections were washed in Tris-buffered saline (TBS) buffer three times followed by incubation in 0.3% hydrogen peroxide in TBS for 10 min at room temperature. After three washes in TBS, sections were blocked with 3% milk in 0.25%

TBS-X (Triton X-100) for 30 min followed by incubation at 4°C overnight with biotinylated AT8 antibody (Thermo Scientific, catalog no. 1020B, 1:500 solution). The next day, after washing three times with TBS, all sections were treated at room temperature for 60 min with reagents included in the VECTASTAIN Elite ABC-HRP Kit, followed by three washes in TBS. Finally, sections were developed and stained using ImmPACT DAB EqV Peroxidase Substrate. Slides were cover-slipped with cytochrome 60 and scanned using a NanoZoomer microscope at 20X magnification. Images were extracted by using the NDP viewer and analyzed with ImageJ software (National Institutes of Health, Bethesda, Maryland, USA, <https://imagej.nih.gov/ij/>).

For immunofluorescence, sections were washed in TBS three times (5 min/cycle). After washing, sections were blocked with a solution containing 3% BSA and 3% normal donkey serum in 0.25% TBS-X for 1 hour at room temperature, followed by an overnight incubation at 4°C with primary antibodies [mouse GFAP (EMD Millipore, MAB3402, 1:1000), rabbit Iba1: Wako, (1:2000); rat CD68 (SeroTec, 1:500)]. The next day, after three washes in TBS, slides were incubated with fluorescently labeled secondary antibodies (Molecular Probes, 1:500) for one hour at room temperature. Sections were washed and incubated with 0.1% Sudan black solution in 70% ethanol for 10 min, washed once more, and mounted in ProLong Gold Antifade mounting medium (Molecular Probes, P36931). Images were obtained by using a Leica Stellaris 5 confocal microscope and analyzed with ImageJ software.

Brain tissue sample processing for enzyme-linked immunosorbent assay (ELISA)

Mouse posterior cortex was sequentially processed in (i) RAB buffer (100 mM MES, 1 mM EGTA, 0.5 mM MgSO_4 , 750 mM NaCl, 20 mM NaF, 1 mM Na_3VO_4 , pH 7.0) supplemented with protease inhibitors (Complete, Roche) and phosphatase inhibitors (PhosSTOP, Roche); (ii) RIPA buffer (150 mM NaCl, 50 mM Tris, 0.5% deoxycholic acid, 1% Triton X-100, 0.1% SDS, 5 mM EDTA, 20 mM NaF, 1 mM Na_3VO_4 , pH 8.0) supplemented by Complete and PhosSTOP; and (iii) 70% formic acid buffer as previously described (8). The tissue was then weighed and homogenized using a pestle (10 μL RAB buffer/1 mg tissue). After centrifugation at 50,000 $\times g$ for 20 min, the supernatant was taken as the RAB-soluble fraction, and the pellet was dissolved in RIPA buffer (10 μL buffer/1 mg tissue) by sonication (1 min at 20% pulse, 1 s interval; Fisher scientific FB120, Pittsburgh, PA). After centrifugation at 50,000 $\times g$ for 20 min, the supernatant was taken as the RIPA-soluble fraction. The pellet was sonicated (1 min at 20% pulse, 1 s interval) in 70% formic acid (10 μL /1 mg tissue) and

centrifuged at 50,000 $\times g$ for 20 min. The supernatant was taken as the formic acid-soluble fraction. All fractions were stored in -80°C until they were analyzed.

Sandwich ELISA

The levels of human total tau, p-tau, and human ApoE were measured by sandwich ELISA and normalized to tissue weight. TAU-5 (mouse monoclonal, 20 $\mu\text{L}/\text{mL}$) was used as the coating antibody for the human tau ELISA, HJ14.5 (mouse monoclonal, 20 $\mu\text{L}/\text{mL}$) for the p-tau ELISA, and HJ15.3 (mouse monoclonal, 5 $\mu\text{L}/\text{mL}$) for the human ApoE ELISA. Biotinylated HT7 (mouse monoclonal, 200 ng/mL; Thermo Fisher) was used to detect antibodies for the human tau ELISA, biotinylated AT8 (mouse monoclonal, 300 ng/mL) for the p-tau ELISA, and biotinylated HJ15.7 (mouse monoclonal, 150 ng/mL) for the human ApoE ELISA.

Astrocyte morphology analysis

Z-stacks (20 μm) of 4',6-diamidino-2-phenylindole (DAPI)- and GFAP-labeled immunofluorescence images were acquired on a Leica Stellaris 5 confocal microscope with a 40X objective and 1024-pixel by 1024-pixel resolution. Simple Neurite Tracer (SNT; ImageJ plug-in open-source tool) was used to reconstruct tridimensional arbors of GFAP-positive astrocytic main processes by semiautomatic tracing (26). For each mouse, three astrocytes were randomly selected in each section from two separate brain sections on the basis of GFAP-stained structures enclosing a single DAPI-stained nucleus. The six astrocytes chosen from each mouse did not have processes that touched the edges of the field or were truncated. Fully traced astrocytes in SNT were used to obtain morphometric data; i.e., process length, end radius, the number of process branches, the total number of interactions between process branches and radius from Sholl analysis (27), and the volume occupied by the astrocytic process from Convex Hull analysis (28).

Microglia morphology analysis

Z-stacks (20 μm) of Iba1-labeled immunofluorescence images were acquired on an LSM 880 II Airyscan FAST confocal microscope (Zeiss) with a 60X objective, 1.8X zoom, and 1024-pixel by 1024-pixel resolution. For each mouse, a total of four z-stacks of the dentate gyrus region were taken from two separate brain sections. Microglia morphology analysis was performed on three-dimensional (3D) images using Imaris 9.5 software (Bitplane). Morphology was analyzed using the Filament Tracer, with no loops allowed and spot detection mode to determine process start and end points per cell. Process reconstruction was made using the following custom settings: detect new starting points; largest diameter 9.00 μm , seed points 2.00 μm ; remove seed points around

starting points; and diameter of sphere regions: 15 μm . All filament parameters were exported into separate Excel files and used for analyzing the number of process branches, process length, and process volume per cell. Image processing, 3D reconstruction, and data analysis were performed in a blinded manner with regards to the experimental conditions.

Nanostring gene expression assay

RNA was isolated from mouse hippocampus using the RNeasy Mini Kit (QIAGEN, catalog no. 74104). Quality control checks were performed on all samples to determine RNA concentration and integrity (RIN scores > 9.3). For the Nanostring gene expression assay, isolated RNA samples were processed by the Genome Technology Access Core at Washington University, using NanoString's nCounter Neuroinflammation panel (735 genes were detected out of 770 targeted genes). Background noise in the data was corrected to a thresholding count value of 20. Lane-by-lane technical variation was corrected by using the geometric median value of the positive-control set. Gene expression normalization was performed subsequently using the geNorm algorithm to select the optimal housekeeping genes (*Mto1*, *Csnk2a2*, *Aars*, *Supt7l*, *Fam104a*, *Tbp*, *Ccdc127*, *Tada2b*, *Lars*, and *Cnot10*).

Differential gene expression was performed using nSolver 4.0 and the Advanced Analysis 2.0 plugin (NanoString). Fold-change expression and *P* values were calculated by linear regression analysis using negative binomial or log-linear models. *P* values were corrected for multiple comparisons using the Benjamini-Hochberg method. Coexpression analysis was performed using the Weighted Gene Correlation Network Analysis (WGCNA) package in R (29). A soft thresholding power of 8 was selected to calculate the unsigned adjacency for normalized gene counts. Hierarchical clustering of the topological overlap matrix dissimilarity was used to produce a gene dendrogram. Gene modules were identified using a dynamic tree cut with a minimum module size of 20 genes. Eigengenes for each module were calculated, and correlations with dummy-coded APOE genotype or the size of the hippocampus as an index of neurodegeneration level were calculated. GO enrichment analysis was performed using Metascape (30).

snRNA-seq of frozen hippocampal tissue

Frozen hippocampus from $n = 5$ mice of the same genotype and treatment were pooled as a single sample. Samples were selected based on those being closest to the mean values of hippocampal volumes. Tissue was homogenized using a Dounce homogenizer in 1 mL of lysis buffer [10 mM Tris-HCl (pH 7.4), 10 mM NaCl, 3 mM MgCl_2 ; 0.005% NP40; and 0.2 U/mL RNase Inhibitor (prepared using nuclease-free

water and chilled to 4°C)] and incubated on ice for 15 min. A 30-mm MACS SmartStrainer was used to remove cell debris and large clumps, followed by centrifugation at 500 $\times g$ for 5 min at 4°C . After carefully removing the supernatant, the pellet containing nuclei was resuspended with 5 mL of nuclei wash and resuspension buffer (1% BSA plus 0.2 U/mL RNase Inhibitor in 1 X PBS). The cell debris removal step, centrifugation, and resuspension steps were repeated twice. Only 500 μL of nuclei wash and resuspension buffer was added in the last resuspension step. The resulting solution was mixed with 900 μL of Sucrose Cushion Buffer I [prepared by mixing 2.7 mL of Nuclei Pure 2M Sucrose Cushion Solution (MilliporeSigma, St. Louis) with 300 mL Nuclei Pure Sucrose Cushion Solution (MilliporeSigma, St. Louis) and then carefully layered to the top of 500 μL Sucrose Cushion Buffer I in a 2-mL eppendorf tube]. After centrifugation at 13,000 $\times g$ for 45 min at 4°C , the nuclear pellet was resuspended in 500 μL nuclei wash and resuspension buffer. The concentration of nuclei was determined using a Countess instrument (Invitrogen) and DAPI staining. The concentration was adjusted to 1200 nuclei/mL using nuclei wash and resuspension buffer before snRNA-seq.

Isolated nuclei were used for droplet-based snRNA-seq using the Chromium Single Cell 3' Reagent Kit (10x Genomics). Libraries were sequenced using a NovaSeq 6000 instrument (Illumina). Sample demultiplexing, barcode processing, and single-nuclei 3' counting was performed using the Cell Ranger Single-Cell Software Suite (10x Genomics). Cell Ranger count was used to (i) align samples to a custom pre-mRNA reference package (mm10) containing the human *APOE* gene, (ii) quantify reads, and (iii) filter those reads with a quality score below 30.

The Seurat v3 and SoupX R packages were used for subsequent analysis of the datasets (31–33). Contaminating cell-free RNA from each sample group was removed using SoupX. Nuclei with mitochondrial content $> 5\%$ or total gene counts < 200 or > 5000 were removed (Seurat). For each group, the percent of mitochondria was regressed out as a nuisance variable, gene counts were normalized, and variable features identified using the SCTransform function in Seurat. The top 3000 variable genes were used to integrate experimental groups using the PrepSCTIntegration, FindIntegrationAnchors, and IntegrateData commands in Seurat. Principal components analysis (PCA) was performed on the integrated dataset and the first 30 principal components were selected for downstream analysis using FindNeighbors. Clusters were identified using the FindClusters function with a granularity ranging from 0.1 to 1.2. Final clustering was performed using a resolution of 0.3. The

first 30 principal components were passed into UMAP using the RunUMAP command with default parameters. Differential gene expression between each cell cluster and all other clusters was performed on SCT data to identify marker genes for each individual cell cluster. Clusters containing high mitochondrial genome content, or marker genes for more than one broad cell type (i.e., microglia and excitatory neurons) were removed and data were reclustered using the first 30 principal components and a resolution of 0.3. In total, 143,835 nuclei with a median UMI of 2735 and median gene number of 1664 across all 10 experimental groups were used in the final analysis.

Differential gene expression to identify marker genes was again performed using MAST (34), and broad cell types were identified on the basis of known cell type-specific markers. For subclustering analysis, nuclei from astrocyte or microglia clusters were extracted from the dataset, RNA counts were renormalized, and the percentage of mitochondrial genes regressed out using the SCTransform command. PCA analysis was performed and the nuclei reclustered. For astrocytes, in addition to regressing the percentage of mitochondrial genes, the percentage of Gh (growth hormone) and Prl (Prolactin) transcripts were also regressed out due to detection in the TEKO-H₂O treatment group. The first 20 principal components were used, and clustering performed at a resolution of 0.15 (data S5). For microglia, the first 10 PCs were used, and clustering performed at a resolution of 0.1 (data S6). Marker genes for subclusters were identified using MAST (data S5 and S6). The SCTransform function from the Seurat package was used to generate graphs from the data containing log-normalized values (35). Expression level represents the log-normalized values of gene counts. Gene counts for each cell were divided by the total counts for that cell and scaled before natural log transformation. GO enrichment analysis was performed using Metascape (30).

Fluidigm Biomark HD real-time PCR

Hippocampus tissues were used for the gene expression analysis. Samples were selected on the basis of the mean values of hippocampal volumes. RNA was extracted from frozen tissues using RNeasy Mini Kit (Qiagen) and converted to cDNA using the high-capacity RNA-to-cDNA kit from Thermo Fisher and the manufacturer's instructions. Gene expression was carried out using Fluidigm Biomark HD real-time PCR system. Using Taqman primers, gene expression was quantitatively measured after normalization the housekeeping gene, *Gapdh*.

16S rRNA amplicon sequencing and analysis

For bacterial V4-16S rDNA amplicon sequencing, each frozen fecal sample was resuspended

in 500 µl of a phenol:chloroform:isoamyl alcohol mixture (25:24:1), followed by addition of 710 µL of 2X Buffer A (200 mM NaCl, 200 mM Trizma base, 20 mM EDTA) and 20% SDS (500:210). The solution was shaken in a Mini-Beadbeater-96 (BioSpec Products) for 4 min with ~250 µl of 0.1 mm zirconia/silica beads and one 3.97-mm steel ball. After centrifugation at 3220 ×g for 4 min, 420 µL of the resulting aqueous phase was transferred to a well of a 96-well plate. A 100 µL aliquot of the crude extract was mixed with 400 µL of a mixture of Qiagen buffer PM and 3M NaOAc, pH5.5 (675:45), and the mixture was passed through a Qiagen QiaQuick 96 plate by centrifugation at 3220 ×g for 10 min, washed twice with 900 µL of Buffer PE by centrifugation, and finally eluted with 130 µL Buffer EB. Purified DNA was quantified using Invitrogen Quant-iT dsDNA BR kit and normalized to 2 ng/µL. Variable region 4 of the bacterial 16S rRNA gene was amplified by PCR using the following conditions: denaturation (94°C for 2 min) followed by 26 cycles of 94°C for 15 s, 50°C for 30 s, and 68°C for 30 s, followed by incubation at 68°C for 2 min.

Sample-associated 16S rDNA amplicons were quantified, pooled, and subjected to sequencing (Illumina MiSeq instrument, paired-end 250 nt reads). Reads were demultiplexed, trimmed to 200 nucleotides, and merged, followed by removal of chimeric sequences (DADA2 v. 1.13.0). ASVs were generated from demultiplexed paired-end reads with DADA2 and taxonomy was assigned on the basis of the DADA2-formatted training dataset (36). Read quality control and the resolution of ASVs were performed with the dada2 R package (37, 38). ASVs that were not assigned to the kingdom Bacteria were filtered out. The remaining reads were assigned taxonomy using the Ribosomal Database Project (RDP trainset 16/release 11.5) 16S rRNA gene sequence database (38).

Analyses of alpha-diversity (richness, Faith's phylogenetic diversity) and beta-diversity (weighted UniFrac distances) were performed using PhyloSeq and additional R packages (39). Taxa (ASVs) whose relative abundances differed significantly between sample groups were identified by performing pairwise comparisons using DESeq2 and MicrobiotaProcess packages (40). A correlation matrix was generated and plotted as ellipses using the corrplot package (41). R codes to generate 16S rRNA-related results and figures in this manuscript are available at GitHub: https://github.com/shandleyle/neurodegeneration_16S.

GC-MS of SCFAs

SCFAs were quantified by GC-MS using a previously described protocol (42). Cecal contents were weighed and placed in 2 mL glass screw cap vials. Ten microliters of a mixture of

internal standards (20 mM of acetic acid-¹³C₂, D₄, propionic acid-D₆, butyric acid-¹³C₄, lactic acid-3,3,3-D₃, and succinic acid-¹³C₄) was added to each vial, followed by 20 µL of 33% HCl and 1 mL diethyl ether. The solution was vortexed vigorously for 10 min. The two phases were separated by centrifugation (4000 ×g for 5 min). The upper organic layer was transferred into another vial and a second 1 mL diethyl ether extraction was performed. After combining the two ether extracts, a 60 µL aliquot was mixed with 20 µL N-tert-butyltrimethylsilyl-N-methyltrifluoroacetamide (MTBSTFA) in a GC auto-sampler vial with a 200 µL glass insert, and the mixture was incubated for 2 hours at room temperature. Samples were analyzed in a randomized order. Derivatized samples (1 µL) were injected with 15:1 split into an Agilent 7890A GC system coupled with 5975C MS detector (Agilent). Analyses were carried on a HP-5MS capillary column (30 m × 0.25 mm, 0.25 µm film thickness, Agilent J & W Scientific) using electronic impact (70 eV) as ionization mode. Helium was used as a carrier gas at a constant flow rate of 1.26 mL/min, and the solvent delay time was set to 3.5 min. The column head pressure was 10 psi. The temperatures of injector, transfer line, and quadrupole were 270°, 280°, and 150°C, respectively. The GC oven was programmed as follows; 45°C held for 2.25 min, increased to 200°C at a rate of 20°C/min, increased to 300°C at a rate of 100°C/min, and finally held for 3 min. Quantification of SCFA was performed by isotope dilution GC-MS using selected ion monitoring (SIM). For SIM analysis, the m/z for native and labeled molecular peaks for SCFA quantified were 117 and 122 (acetate), 131 and 136 (propionate), 145 and 149 (butyrate), 261 and 264 (lactate), and 289 and 293 (succinate), respectively. Various concentrations of standards were spiked into control samples to prepare the calibration curves for quantification.

Flow cytometry

Mice were given a lethal dose of pentobarbital sodium (Fatal-Plus, Vortech) intraperitoneally and perfused through the heart with ice-cold PBS supplemented with 5 U/mL heparin. The dural meninges and spleen were dissected and digested with 1.4 U/mL of Collagenase VIII (Sigma Aldrich, catalog no. C2139) and 35 U/mL of DNase I (Sigma Aldrich, catalog no. DN25) for 20 to 30 min at 37°C. After the digestion step, the tissue was passed through 70-µm nylon mesh cell strainers (Fisher Scientific). Cells were then centrifuged at 340 ×g for 5 min or 450 ×g for 4 min at 4°C, and then stained in PBS with Zombie NIR Fixable Viability Kit (1:500, BioLegend, catalog no. 423105) for 15 min on ice. After one wash with fluorescence-activated cell sorting (FACS) buffer (PBS with 2% fetal bovine serum or PBS with 1% bovine serum albumin, 2 mM EDTA, 25 mM HEPES)

Fc-receptors were blocked with anti-CD16/32 (1:100, BioLegend, clone 93, catalog no. 101302) for 15 min on ice. An equal volume of primary antibody mix was added, and cells were stained for 20 min on ice at 1:300 final dilution. Samples were then washed twice with FACS buffer and acquired on a spectral flow cytometer (Aurora, Cytex Biosciences). Data were unmixed using Spectral flow software (Cytex) and then gated and quantified using FlowJo v10.8.2 (Treestar).

The following antibodies were used for flow cytometry; anti-CD4 BUV395 (BD, GK1.5, catalog no. 563790), anti-CD5 BUV496 (BD, 53-7.3, catalog no. 741048), anti-CD27 BUV563 (BD, LG.3A10, catalog no. 741275), anti-CD44 BUV615 (BD, IM7, catalog no. 751414), anti-CD11c BUV737 (BioLegend, N418, catalog no. 749039), anti-TCRb BUV805 (BD, H57-597, catalog no. 748405), Ly6G BV421 (BioLegend, 1A8, catalog no. 127628), anti-CD25 Pacific Blue (BioLegend, PC61, catalog no. 102022), anti-CD19 BV480 (BD, 1D3, catalog no. 566107), anti-I-A/I-E BV510 (BioLegend, M5/114.15.2, catalog no. 107641), anti-CXCR3 (eBioscience, CXCR3-173, catalog no. 63-1831), B220 BV650 (BD, RA3-6B2, catalog no. 563893), anti-CD49a BV711 (BD, Ha31/8, catalog no. 564863), anti-CD45 BV750 (BD, 30-F11, catalog no. 746947), anti-Ly-6C AlexaFluor488 (BioLegend, HK1.4, catalog no. 128022), anti-CD8a AlexaFluor532 (eBioscience, 53-6.7m catalog no. 58-0081), anti-CD122 BrilliantBlue700 (BD, TM-b1, catalog no. 742112), CD69 PE (BioLegend, H1.2F3, catalog no. 104508), anti-CD186 (CXCR6) PE-Dazzle 594 (BioLegend, SA051D1, catalog no. 151117), anti-CD127 PE-Cy5 (BioLegend, A7R34, catalog no. 135016), anti-NK1.1 PE-Cy7 (eBioscience, PK136, catalog no. 108714), anti-TCRg/d Alexa-Fluor647 (BioLegend, GL3, catalog no. 118134), and anti-F4/80 AlexaFluor700 (BioLegend, BM8, catalog no. 123130).

FACS for lung macrophage isolation

Lung samples were harvested from the mice and chopped up with scissors into 1- to 2-mm sizes. The sliced lung samples were digested in digestion buffer containing 50 U/mL DNase (Sigma), 100 U/mL Hyaluronidase (Sigma), and 0.28 U/mL Liberase (Roche) at 37°C for 45 min. The mixtures were gently inverted a few times every 5 to 10 min. A final concentration of 10% FBS was used to stop the reaction and the samples were smashed through a 70-µm-diameter cell strainer. The cell suspensions were pelleted down by centrifugation at 456 ×g for 5 min. Red blood cells were removed with 5 mL ACK buffer (150 mM ammonium chloride, 10 mM potassium bicarbonate, and 0.1 mM EDTA) at room temperature for 2 min. The reaction was stopped by adding 1 mL of FBS, and cells were passed through a 70-µm strainer one more time. Cells were pelleted and ~5 × 10⁶ cells were used for staining.

Cell sorting was completed on a FACS AriaII. Staining was performed at 4°C in the presence of Fc block (2.4G2; Leinco) in magnetic-activated cell-sorting (MACS) buffer (PBS + 0.5% BSA + 2 mM EDTA). The following antibodies were used from Biolegend: BV510 anti-CD45 (30-F11), APC-Cy7 anti-CD11b (M1/70), Pacific-Blue anti-MHC-II (I-A/I-E) (M5/114.15.2), PercP-Cy5.5 anti-Ly6C/Ly6G (Gr-1) (RB6-8C5), and APC anti-CD64 (X54-5/7.1). Antibodies obtained from Invitrogen included: PE-Cy7 anti-CD11c (N418) and PE anti-SiglecF (1RNM44N). The alveolar macrophages were sorted as CD45+ SiglecF+ CD11c+ CD64+ CD11b^{lo} cells.

RNA-seq and analysis

RNA was extracted from FACS-sorted lung macrophages (described above) using the RNeasy Plus Micro Kit (QIAGEN, catalog no. 74034). RNA samples were prepared according to library kit manufacturer's protocol, indexed, pooled, and sequenced on an Illumina Nova-Seq 6000. Basecalls and demultiplexing were performed with Illumina's bcl2fastq2 software. RNA-seq reads were then aligned and quantitated to the Ensemble release 101 primary assembly with an Illumina DRAGEN Bio-IT on-premise server running version 3.9.3-8 software.

All gene counts were then imported into the R/Bioconductor package EdgeR and TMM normalization size factors were calculated to adjust for samples for differences in library size (43). Ribosomal genes and genes not expressed in the smallest group size minus one sample greater than one count-per-million were excluded from further analysis. The TMM size factors and the matrix of counts were then imported into the R/Bioconductor package Limma (44). Weighted likelihoods based on the observed mean-variance relationship of every gene and sample were then calculated for all samples and the count matrix was transformed to moderated log₂ counts-per-million with Limma's voomWithQualityWeights (45). The performance of all genes was assessed with plots of the residual standard deviation of every gene to their average log-count with a robustly fitted trend line of the residuals. Differential expression analysis was then performed to analyze for differences between conditions; the results were filtered for only those genes with Benjamini-Hochberg false-discovery rate adjusted *P* values ≤ 0.05. GO enrichment analysis was performed using Metascape (30).

Quantification and statistical analysis

All data were expressed as mean values ± SEMs. Statistical analysis was performed with JMP15 Pro (SAS Institute, Cary, NC, RRID: SCR_014242) and GraphPad Prism 9. Means between two groups were compared with a

two-tailed, unpaired Student's *t* test. Comparisons of means from three groups with each other were analyzed with one-way analysis of variance (ANOVA). Two-way ANOVAs were used to analyze between-subjects designs with two variable factors. Repeated-measures designs were analyzed using mixed-effects restricted maximum likelihood (REML) model. Tukey was used for post hoc pairwise comparisons. Fisher's exact test was used to analyze probability distributions. The strength of the linear relationship between two different variables was analyzed using Pearson's or Spearman's correlation. The null hypothesis was rejected at the *P* < 0.05 level. Statistical significance was taken as **P* < 0.05, ***P* < 0.01, and ****P* < 0.001. Statistical significance of the main effects without the interactions of two variables was indicated as #*P* < 0.05, ##*P* < 0.01, and ###*P* < 0.001. All statistical information is listed in table S1.

REFERENCES AND NOTES

1. J. M. Long, D. M. Holtzman, Alzheimer Disease: An Update on Pathobiology and Treatment Strategies. *Cell* **179**, 312–339 (2019). doi: [10.1016/j.cell.2019.09.001](https://doi.org/10.1016/j.cell.2019.09.001); pmid: [31564456](https://pubmed.ncbi.nlm.nih.gov/31564456/)
2. D. O. Seo, D. M. Holtzman, Gut Microbiota: From the Forgotten Organ to a Potential Key Player in the Pathology of Alzheimer's Disease. *J. Gerontol. A Biol. Sci. Med. Sci.* **75**, 1232–1241 (2020). doi: [10.1093/gerona/glz262](https://doi.org/10.1093/gerona/glz262); pmid: [31738402](https://pubmed.ncbi.nlm.nih.gov/31738402/)
3. T. Harach et al., Reduction of Abeta amyloid pathology in APPPS1 transgenic mice in the absence of gut microbiota. *Sci. Rep.* **7**, 41802 (2017). doi: [10.1038/srep41802](https://doi.org/10.1038/srep41802); pmid: [28176819](https://pubmed.ncbi.nlm.nih.gov/28176819/)
4. H. B. Dodiya et al., Sex-specific effects of microbiome perturbations on cerebral Aβ amyloidosis and microglia phenotypes. *J. Exp. Med.* **216**, 1542–1560 (2019). doi: [10.1084/jem.20182386](https://doi.org/10.1084/jem.20182386); pmid: [31097468](https://pubmed.ncbi.nlm.nih.gov/31097468/)
5. I. J. Parikh et al., Murine Gut Microbiome Association With APOE Alleles. *Front. Immunol.* **11**, 200 (2020). doi: [10.3389/fimmu.2020.00200](https://doi.org/10.3389/fimmu.2020.00200); pmid: [32117315](https://pubmed.ncbi.nlm.nih.gov/32117315/)
6. T. T. T. Tran et al., APOE genotype influences the gut microbiome structure and function in humans and mice: Relevance for Alzheimer's disease pathophysiology. *FASEB J.* **33**, 8221–8231 (2019). doi: [10.1096/fj.201900071R](https://doi.org/10.1096/fj.201900071R); pmid: [30958695](https://pubmed.ncbi.nlm.nih.gov/30958695/)
7. C. Wang et al., Selective removal of astrocytic APOE4 strongly protects against tau-mediated neurodegeneration and decreases synaptic phagocytosis by microglia. *Neuron* **109**, 1657–1674.e7 (2021). doi: [10.1016/j.neuron.2021.03.024](https://doi.org/10.1016/j.neuron.2021.03.024); pmid: [33831349](https://pubmed.ncbi.nlm.nih.gov/33831349/)
8. Y. Shi et al., ApoE4 markedly exacerbates tau-mediated neurodegeneration in a mouse model of tauopathy. *Nature* **549**, 523–527 (2017). doi: [10.1038/nature24016](https://doi.org/10.1038/nature24016); pmid: [28959956](https://pubmed.ncbi.nlm.nih.gov/28959956/)
9. Y. Shi et al., Microglia drive APOE-dependent neurodegeneration in a tauopathy mouse model. *J. Exp. Med.* **216**, 2546–2561 (2019). doi: [10.1084/jem.20190980](https://doi.org/10.1084/jem.20190980); pmid: [31601677](https://pubmed.ncbi.nlm.nih.gov/31601677/)
10. R. Mancuso et al., CSFIR inhibitor JNJ-40346527 attenuates microglial proliferation and neurodegeneration in P301S mice. *Brain* **142**, 3243–3264 (2019). doi: [10.1093/brain/awz241](https://doi.org/10.1093/brain/awz241); pmid: [31504240](https://pubmed.ncbi.nlm.nih.gov/31504240/)
11. C. N. Mann et al., Astrocytic α2-Na⁺/K⁺ ATPase inhibition suppresses astrocyte reactivity and reduces neurodegeneration in a tauopathy mouse model. *Sci. Transl. Med.* **14**, eabm4107 (2022). doi: [10.1126/scitranslmed.abm4107](https://doi.org/10.1126/scitranslmed.abm4107); pmid: [35171651](https://pubmed.ncbi.nlm.nih.gov/35171651/)
12. D. Erny et al., Host microbiota constantly control maturation and function of microglia in the CNS. *Nat. Neurosci.* **18**, 965–977 (2015). doi: [10.1038/nn.4030](https://doi.org/10.1038/nn.4030); pmid: [26030851](https://pubmed.ncbi.nlm.nih.gov/26030851/)
13. S. Spichak et al., Microbially-derived short-chain fatty acids impact astrocyte gene expression in a sex-specific manner.

- Brain Behav. Immun. Health* **16**, 100318 (2021). doi: [10.1016/j.bbih.2021.100318](https://doi.org/10.1016/j.bbih.2021.100318); pmid: [34589808](https://pubmed.ncbi.nlm.nih.gov/34589808/)
14. T. R. Sampson *et al.*, Gut Microbiota Regulate Motor Deficits and Neuroinflammation in a Model of Parkinson's Disease. *Cell* **167**, 1469–1480.e12 (2016). doi: [10.1016/j.cell.2016.11.018](https://doi.org/10.1016/j.cell.2016.11.018); pmid: [27912057](https://pubmed.ncbi.nlm.nih.gov/27912057/)
 15. P. Jirkof, Burrowing and nest building behavior as indicators of well-being in mice. *J. Neurosci. Methods* **234**, 139–146 (2014). doi: [10.1016/j.jneumeth.2014.02.001](https://doi.org/10.1016/j.jneumeth.2014.02.001); pmid: [24525328](https://pubmed.ncbi.nlm.nih.gov/24525328/)
 16. I. D. Vainchtein, A. V. Molofsky, Astrocytes and Microglia: In Sickness and in Health. *Trends Neurosci.* **43**, 144–154 (2020). doi: [10.1016/j.tins.2020.01.003](https://doi.org/10.1016/j.tins.2020.01.003); pmid: [32044129](https://pubmed.ncbi.nlm.nih.gov/32044129/)
 17. R. Di Marco Barros, Z. Fitzpatrick, M. R. Clatworthy, The gut-meningeal immune axis: Priming brain defense against the most likely invaders. *J. Exp. Med.* **219**, e20211520 (2022). doi: [10.1084/jem.20211520](https://doi.org/10.1084/jem.20211520); pmid: [35195681](https://pubmed.ncbi.nlm.nih.gov/35195681/)
 18. K. Alves de Lima *et al.*, Meningeal $\gamma\delta$ T cells regulate anxiety-like behavior via IL-17a signaling in neurons. *Nat. Immunol.* **21**, 1421–1429 (2020). doi: [10.1038/s41590-020-0776-4](https://doi.org/10.1038/s41590-020-0776-4); pmid: [32929273](https://pubmed.ncbi.nlm.nih.gov/32929273/)
 19. M. Colonna, G. Trinchieri, Y. J. Liu, Plasmacytoid dendritic cells in immunity. *Nat. Immunol.* **5**, 1219–1226 (2004). doi: [10.1038/nri1141](https://doi.org/10.1038/nri1141); pmid: [15549123](https://pubmed.ncbi.nlm.nih.gov/15549123/)
 20. T. J. Schuijt *et al.*, The gut microbiota plays a protective role in the host defence against pneumococcal pneumonia. *Gut* **65**, 575–583 (2016). doi: [10.1136/gutjnl-2015-309728](https://doi.org/10.1136/gutjnl-2015-309728); pmid: [26511795](https://pubmed.ncbi.nlm.nih.gov/26511795/)
 21. Y. Sun *et al.*, The Gut Microbiome as a Therapeutic Target for Cognitive Impairment. *J. Gerontol. A Biol. Sci. Med. Sci.* **75**, 1242–1250 (2020). doi: [10.1093/gerona/gtz281](https://doi.org/10.1093/gerona/gtz281); pmid: [31811292](https://pubmed.ncbi.nlm.nih.gov/31811292/)
 22. D. O. Seo, B. D. Boros, D. M. Holtzman, The microbiome: A target for Alzheimer disease? *Cell Res.* **29**, 779–780 (2019). doi: [10.1038/s41422-019-0227-7](https://doi.org/10.1038/s41422-019-0227-7); pmid: [31488883](https://pubmed.ncbi.nlm.nih.gov/31488883/)
 23. T. V. Huynh *et al.*, Lack of hepatic apoE does not influence early A β deposition: Observations from a new APOE knock-in model. *Mol. Neurodegener.* **14**, 37 (2019). doi: [10.1186/s13024-019-0337-1](https://doi.org/10.1186/s13024-019-0337-1); pmid: [31623648](https://pubmed.ncbi.nlm.nih.gov/31623648/)
 24. A. T. Stefká *et al.*, Commensal bacteria protect against food allergen sensitization. *Proc. Natl. Acad. Sci. U.S.A.* **111**, 13145–13150 (2014). doi: [10.1073/pnas.1412008111](https://doi.org/10.1073/pnas.1412008111); pmid: [25151757](https://pubmed.ncbi.nlm.nih.gov/25151757/)
 25. R. M. Deacon, Assessing nest building in mice. *Nat. Protoc.* **1**, 1117–1119 (2006). doi: [10.1038/nprot.2006.170](https://doi.org/10.1038/nprot.2006.170); pmid: [17406392](https://pubmed.ncbi.nlm.nih.gov/17406392/)
 26. G. Tavares *et al.*, Employing an open-source tool to assess astrocyte tridimensional structure. *Brain Struct. Funct.* **222**, 1989–1999 (2017). doi: [10.1007/s00429-016-1316-8](https://doi.org/10.1007/s00429-016-1316-8); pmid: [27696155](https://pubmed.ncbi.nlm.nih.gov/27696155/)
 27. D. A. Sholl, Dendritic organization in the neurons of the visual and motor cortices of the cat. *J. Anat.* **87**, 387–406 (1953). pmid: [13117757](https://pubmed.ncbi.nlm.nih.gov/13117757/)
 28. M. Augusto-Oliveira *et al.*, Plasticity of microglia. *Biol. Rev.* **97**, 217–250 (2022). doi: [10.1111/brv.12797](https://doi.org/10.1111/brv.12797); pmid: [34549510](https://pubmed.ncbi.nlm.nih.gov/34549510/)
 29. P. Langfelder, S. Horvath, WGCNA: An R package for weighted correlation network analysis. *BMC Bioinformatics* **9**, 559 (2008). doi: [10.1186/1471-2105-9-559](https://doi.org/10.1186/1471-2105-9-559); pmid: [19114008](https://pubmed.ncbi.nlm.nih.gov/19114008/)
 30. Y. Zhou *et al.*, Metascape provides a biologist-oriented resource for the analysis of systems-level datasets. *Nat. Commun.* **10**, 1523 (2019). doi: [10.1038/s41467-019-09234-6](https://doi.org/10.1038/s41467-019-09234-6); pmid: [30944313](https://pubmed.ncbi.nlm.nih.gov/30944313/)
 31. A. Butler, P. Hoffman, P. Smibert, E. Papalexi, R. Satija, Integrating single-cell transcriptomic data across different conditions, technologies, and species. *Nat. Biotechnol.* **36**, 411–420 (2018). doi: [10.1038/nbt.4096](https://doi.org/10.1038/nbt.4096); pmid: [29608179](https://pubmed.ncbi.nlm.nih.gov/29608179/)
 32. T. Stuart *et al.*, Comprehensive Integration of Single-Cell Data. *Cell* **177**, 1888–1902.e21 (2019). doi: [10.1016/j.cell.2019.05.031](https://doi.org/10.1016/j.cell.2019.05.031); pmid: [31178118](https://pubmed.ncbi.nlm.nih.gov/31178118/)
 33. M. D. Young, S. Behjati, SoupX removes ambient RNA contamination from droplet-based single-cell RNA sequencing data. *Gigascience* **9**, giaa151 (2020). doi: [10.1093/gigascience/giaa151](https://doi.org/10.1093/gigascience/giaa151); pmid: [33367645](https://pubmed.ncbi.nlm.nih.gov/33367645/)
 34. G. Finak *et al.*, MAST: A flexible statistical framework for assessing transcriptional changes and characterizing heterogeneity in single-cell RNA sequencing data. *Genome Biol.* **16**, 278 (2015). doi: [10.1186/s13059-015-0844-5](https://doi.org/10.1186/s13059-015-0844-5); pmid: [26653891](https://pubmed.ncbi.nlm.nih.gov/26653891/)
 35. C. Hafemeister, R. Satija, Normalization and variance stabilization of single-cell RNA-seq data using regularized negative binomial regression. *Genome Biol.* **20**, 296 (2019). doi: [10.1186/s13059-019-1874-1](https://doi.org/10.1186/s13059-019-1874-1); pmid: [31870423](https://pubmed.ncbi.nlm.nih.gov/31870423/)
 36. B. J. Callahan *et al.*, DADA2: High-resolution sample inference from Illumina amplicon data. *Nat. Methods* **13**, 581–583 (2016). doi: [10.1038/nmeth.3869](https://doi.org/10.1038/nmeth.3869); pmid: [27214047](https://pubmed.ncbi.nlm.nih.gov/27214047/)
 37. J. R. Cole *et al.*, Ribosomal Database Project: Data and tools for high throughput rRNA analysis. *Nucleic Acids Res.* **42**, D633–D642 (2014). doi: [10.1093/nar/gkt1244](https://doi.org/10.1093/nar/gkt1244); pmid: [24288368](https://pubmed.ncbi.nlm.nih.gov/24288368/)
 38. P. J. McMurdie, S. Holmes, phyloseq: An R package for reproducible interactive analysis and graphics of microbiome census data. *PLOS ONE* **8**, e61217 (2013). doi: [10.1371/journal.pone.0061217](https://doi.org/10.1371/journal.pone.0061217); pmid: [23630581](https://pubmed.ncbi.nlm.nih.gov/23630581/)
 39. M. I. Love, W. Huber, S. Anders, Moderated estimation of fold change and dispersion for RNA-seq data with DESeq2. *Genome Biol.* **15**, 550 (2014). doi: [10.1186/s13059-014-0550-8](https://doi.org/10.1186/s13059-014-0550-8); pmid: [25516281](https://pubmed.ncbi.nlm.nih.gov/25516281/)
 40. S. Xu, G. Yu, MicrobiotaProcess: An R Package for Analysis, Visualization and Biomarker Discovery of Microbiome, version 0.84 (2021).
 41. T. Wei, V. R. Simko, R package “corrplot”: Visualization of a Correlation Matrix (2021).
 42. F. E. Rey *et al.*, Metabolic niche of a prominent sulfate-reducing human gut bacterium. *Proc. Natl. Acad. Sci. U.S.A.* **110**, 13582–13587 (2013). doi: [10.1073/pnas.1312524110](https://doi.org/10.1073/pnas.1312524110); pmid: [23898195](https://pubmed.ncbi.nlm.nih.gov/23898195/)
 43. M. D. Robinson, D. J. McCarthy, G. K. Smyth, edgeR: A Bioconductor package for differential expression analysis of digital gene expression data. *Bioinformatics* **26**, 139–140 (2010). doi: [10.1093/bioinformatics/btp616](https://doi.org/10.1093/bioinformatics/btp616); pmid: [19910308](https://pubmed.ncbi.nlm.nih.gov/19910308/)
 44. M. E. Ritchie *et al.*, limma powers differential expression analyses for RNA-sequencing and microarray studies. *Nucleic Acids Res.* **43**, e47 (2015). doi: [10.1093/nar/gkv007](https://doi.org/10.1093/nar/gkv007); pmid: [25605792](https://pubmed.ncbi.nlm.nih.gov/25605792/)
 45. R. Liu *et al.*, Why weight? Modelling sample and observational level variability improves power in RNA-seq analyses. *Nucleic Acids Res.* **43**, e97 (2015). doi: [10.1093/nar/gkv412](https://doi.org/10.1093/nar/gkv412); pmid: [25925576](https://pubmed.ncbi.nlm.nih.gov/25925576/)
- ACKNOWLEDGMENTS**
- We thank C. Nagler and her laboratory members at the University of Chicago for the discussion about the antibiotic treatment protocol; M. Colonna, Y. Shi, C. Wang, A. Cashikar, J. Long, N. Griffin, M. Cella, S. Wagoner, M. Hibberd, and K. de Lima at Washington University for technical discussions; J. Stanley, B. Boros, J. Serugo, S. Venkatesh, K. Mihindukulasuriya, and L. Wang for technical assistance; D. Bender at CHiIPs (Center for Human Immunology and Immunotherapy Programs at Washington University) for performing multiplex cytokine assay; and C. Sawyer, C. Markovic, T. Sinnwell, E. Tycksen, and others at GTAC (Genome Technology Access Center at Washington University) for their contributions to generating genomic and transcriptomic datasets. **Funding:** This study was supported by Good Ventures (D.M.H.) and National Institutes of Health grant NS090934 (D.M.H.). **Author contributions:** D.S. played a primary role in conceiving this study, developing experimental methods, performing experiments, analyzing the resulting datasets, and writing the original draft manuscript. D.O. and M.K. generated and maintained GF mice. N.J. analyzed microglial cell morphology. J.D.U. analyzed snRNA-seq data. M.M. extracted DNA from fecal samples and oversaw V4-16S rRNA amplicon sequencing. Y.L., C.D., and S.A.H. analyzed the resulting 16S rRNA datasets. J.H., M.L., and J.K. performed flow cytometry. H.H. isolated lung macrophages. J.R.S. and X.B. collected brain, cecum, and plasma samples. E.F. quantified imaging data. J.C. and S.D. performed metabolomic analyses. J.L.-G., S.S.S., and J.I.G. conceptualized experiments and their design. D.M.H. conceptualized, acquired funding for, and supervised the project. J.I.G. and D.M.H. edited the final manuscript. **Competing interests:** D.M.H. is a cofounder of C2N Diagnostics, LLC, and is on the scientific advisory board and/or consults for Genentech, Denali, C2N Diagnostics, Cajal Neurosciences, and Alector. D.M.H. is an inventor on a patent licensed by Washington University to C2N Diagnostics on the therapeutic use of anti-tau antibodies and a patent licensed by Washington University to Eli Lilly on a humanized anti-A β antibody. The Holtzman laboratory receives research grants from the National Institutes of Health, Cure Alzheimer's Fund, the Rainwater Foundation, the JPB Foundation, Good Ventures, Novartis, Eli Lilly, and NextCure. The authors declare no other competing interests. **Data and materials availability:** snRNA-seq datasets have been deposited in the Gene Expression Omnibus under accession no. GSE213446. 16S rDNA amplicon sequencing datasets have been deposited in the European Nucleotide Archive under accession no. PRJEB55869. **License information:** Copyright © 2023 the authors, some rights reserved; exclusive licensee American Association for the Advancement of Science. No claim to original US government works. <https://www.science.org/about/science-licenses-journal-article-reuse>
- SUPPLEMENTARY MATERIALS**
- science.org/doi/10.1126/science.add1236
 Figs. S1 to S18
 Table S1
 MDAR Reproducibility Checklist
 Data S1 to S8
- [View/request a protocol for this paper from Bio-protocol.](#)
- Submitted 22 May 2022; resubmitted 10 October 2022
 Accepted 22 November 2022
[10.1126/science.add1236](https://doi.org/10.1126/science.add1236)